Computational Studies of Halide and Hybrid Perovskite Materials for Solar Cells

Walsh Atkins, Philip

Award date:
2018

Awarding institution:
University of Bath

Computational Studies of Halide and Hybrid Perovskite Materials for Solar Cells

Philip Walsh Atkins

A thesis presented for the degree of
Master of Philosophy

Department of Chemistry
University of Bath

September 2017

Declaration

This thesis/portfolio may be made available for consultation within the University Library and may be photocopied or lent to other libraries for the purposes of consultation with effect from.....

Signed on behalf of the Faculty/School of.....

Abstract

Halide perovskites have rapidly become materials of great interest in the photovoltaic community, due largely to their high efficiencies and the rapid pace at which the efficiency of perovskite solar cells is increasing. The main focus of work has been on the organic-inorganic hybrid perovskite methylammonium lead iodide $CH_3NH_3PbI_3$, often known as MAPI, which shows great promise for a new generation of photovoltaics. As the search for more efficient cells progresses, mixed 'A' site cation cells have come to the forefront of research, with efficiencies reaching over 20 %. The fully inorganic perovskite $CsPbI_3$ has been proposed as an alternative to MAPI and also shows great promise, although the viability of $CsPbI_3$ for use in solar cells remains to be conclusively demonstrated. Another alternative to MAPI is the formamidinium ($CH(NH_2)_2^+$) analogue FAPI. The highest efficiency cells use FAPI as a dopant with small quantities of smaller methylammonium, caesium and rubidium cations doped onto the 'A' site. Computer modelling techniques have been used and a potential model has been developed which accurately reproduces all the observed structures in the $Cs(Pb,Sn)(I,Br,Cl)_3$ series. The developed potential model simulates all the phases in the examined series to a high degree of accuracy. The potential model was then used to examine the effect of varying the Cs cation size on the relative stabilities of both the perovskite and non-perovskite phases of $CsPbI_3$. In addition, *ab initio* molecular dynamics simulations have been carried out on the doped FAPI structures, revealing at the atomic scale the behaviour which drives their high efficiencies. The effect of cation doping on octahedral tilting and locking was studied, showing how incorporation of small cations can cause fundamental changes in the dynamics of the structure, boosting it's stability and efficiency.

For Richard

Acknowledgements

First and foremost I would like to thank Dr Chris Eames and Professor Saiful Islam for all their help and guidance over the last two years, including helping to direct the project and writing some of the codes used during the project. I would also like to thank Jenny, Jess, Hungru, James, Piero, and Eszter for all their assistance and always being entertaining. Additionally I would like to thank Professor Steve Parker and the Parker group, Professor Alison Walker and Dr Dibya Ghosh. Various people have helped me proof read and to craft this thesis, some willingly, so I should probably also thank them.

I would like to thank all my family and friends who have supported me through this period of prolonged madness. Thanks to my parents, to Nick, and to Charlotte for all their support. Thanks also to Tom, Andy, Matt, Drew, Adam, Alex, Rob, Sam, Giles, and everyone at 66^{th}.

I would also like to thank the Balena HPC service, the MCC for access to the ARCHER HPC facility, and the EMCS consortium. This work was undertaken with funding from the EPSRC.

"A learning experience is one of those things that says,
'You know that thing you just did? Don't do that.'"

Douglas Adams

The Salmon of Doubt

List of Figures

List of Tables

List of Presentations and Publications

Publication

- Dibyajyoti Ghosh, Philip Walsh Atkins, M. Saiful Islam, Alison Walker and Christopher Eames, *Good Vibrations: Locking of Octahedral Tilting in Mixed-Cation Iodide Perovskites for Solar Cells*, ACS Energy Letters, 2017, **2 (10)**, 2424–2429

Presentations

- **March 2016:** ABXPV conference, Barcelona, Spain

  Poster: Inorganic Halide Perovskites: What Are The Ion Migration Properties?

- **May 2016:** Chemistry PG Symposium, Bath

  Poster: Inorganic Halide Perovskites for Solar Cells: Stabilising the Ideal Phase

- **March 2017:** Department of Chemistry Postgraduate Talks

  Talk: Hybrid Halide Perovskites for Solar Cells

- **July 2017:** MC13 Conference, Liverpool

  Poster: Good Vibrations: Locking of Octahedral Tilting in Mixed-Cation Iodide Perovskites for Solar Cells

- **September 2017:** EMCS Symposium, Bath

  Poster: Good Vibrations: Locking of Octahedral Tilting in Mixed-Cation Iodide Perovskites for Solar Cells

Contents

Chapter 1

Introduction

"See first, think later, then test. But always see first. Otherwise, you will only see what you were expecting. Most scientists forget that."

Wonko the Sane

So Long, and Thanks for All the Fish

The search for new photovoltaic materials is a rapidly developing area of research in materials science. As fossil fuels become less abundant and the demand for clean, renewable energy grows, advancement in new energy generation technologies is of greater interest than ever before. Aiming to generate electricity in a sustainable manner without the carbon emissions of fossil fuels, technologies such as wind, hydroelectric and solar have all been developed as alternative and less damaging power sources.

Many renewable technologies, although able to produce large amounts of clean electricity, have significant downsides such as efficiency and the need for energy storage. A single wind turbine can only produce a limited amount of electricity, so a large wind farm is needed to produce enough electricity to power a town or city. This takes up large amounts of space. Solar power only generates power during the day while it is sunny, and improvements the efficiency of the cells and energy storage are needed. Additionally there is a large upfront energy requirement in the manufacturing of solar cells.[1]

Despite these issues, photovoltaics in particular have several advantages which stand them out as promising candidates for future renewable energy

production. Being silent and without mechanical parts means that they can more easily be integrated into towns and cities, without the obvious downsides of wind power. They are also able to be installed on buildings and roofs with ease. This means that despite the amount of space required, the large area needed does not have to be solely used for power generation. Unlike power sources such as hydroelectric power, they can be installed anywhere which gets good sunlight and are not constrained by the geography of the area, and unlike nuclear power they do not generate large quantities of dangerous waste. All of these advantages mean that solar power is a promising technology and of considerable interest in materials science as the technology is further improved.

1.1 Principles of Solar Cell Operation

Solar cells convert light into electricity via the photovoltaic effect. The photovoltaic effect is an absorption of energy by the material's valence band electrons producing an excitation in the conduction band, which in turn can be harnessed to produce energy. A solar cell architecture generally consists of a set of layers sandwiched together. Normally a glass layer through which light can pass through, a semiconducting absorber layer which produces charges, and front/back electrodes. The top contact is generally layered on top of the glass, as shown in Figure 1.1 to create the contact. Some solar cells also contain a buffer layer to improve performance or efficiency.

Within the solar cell, an incident photon from sunlight is absorbed by a semiconducting absorber layer such as silicon. The incident photon then excites electrons from the valence band to the conduction band of the semiconductor, which facilitates the electrical conductivity of the system via charge carriers. The charge carriers in the system are free electrons and electron holes. An electron in the conduction band can freely move throughout the semiconductor, migrating through the system towards anodes and cathodes layered around the semiconductor, and into an external circuit. An electron hole is the vacancy produced in the valence band by the excited electron. These two charge carriers then migrate round the circuit in the solar cell, producing electricity.

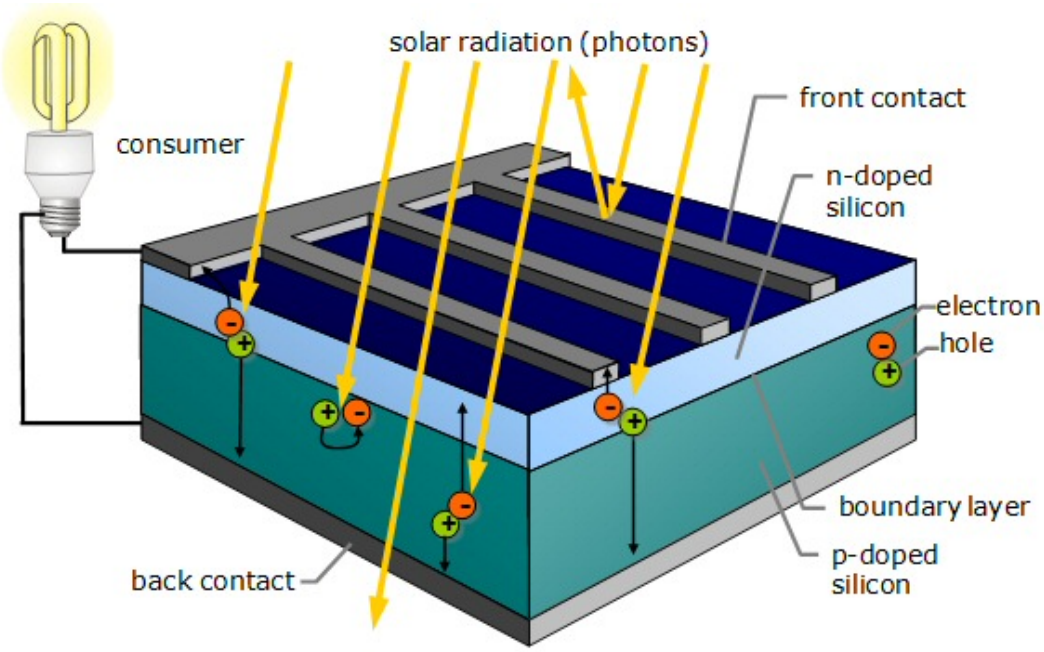

Figure 1.1: A schematic of a solar cell with doped silicon as the semiconducting (absorber) layer. From http://www.stelr.org.au/solar-cells/ (Accessed January 2017)

The semiconducting layer in the solar cell in Figure 1.1 is doped silicon, with p and n-doping facilitating the charge transport. p-type doping of silicon with group III elements such as boron creates additional electron holes, increasing the conductivity of the system by increasing the number of charge carriers. N-type doping with group V elements such as phosphorus introduces additional electrons into the system, also increasing the conductivity.

Figure 1.2 shows how these p and n-type semiconductors work together in the cell, creating additional charge carriers and also tuning the band gap for electron excitation and electron-hole recombination.

In an ideal solar cell, the band gap between the valence and conduction bands in the semiconductor is smaller than the energy of the incident photon, which allows the excited electron to gain enough energy to cross the gap. This means the efficiency of a solar cell is primarily governed by the band gap of the semiconductor, and whether the band gap is direct or indirect.

A semiconductor having an indirect band gap means that the maximum energy state of the valence band and the minimum energy state of the conduction band have different crystalline momentum, and an electron cannot shift

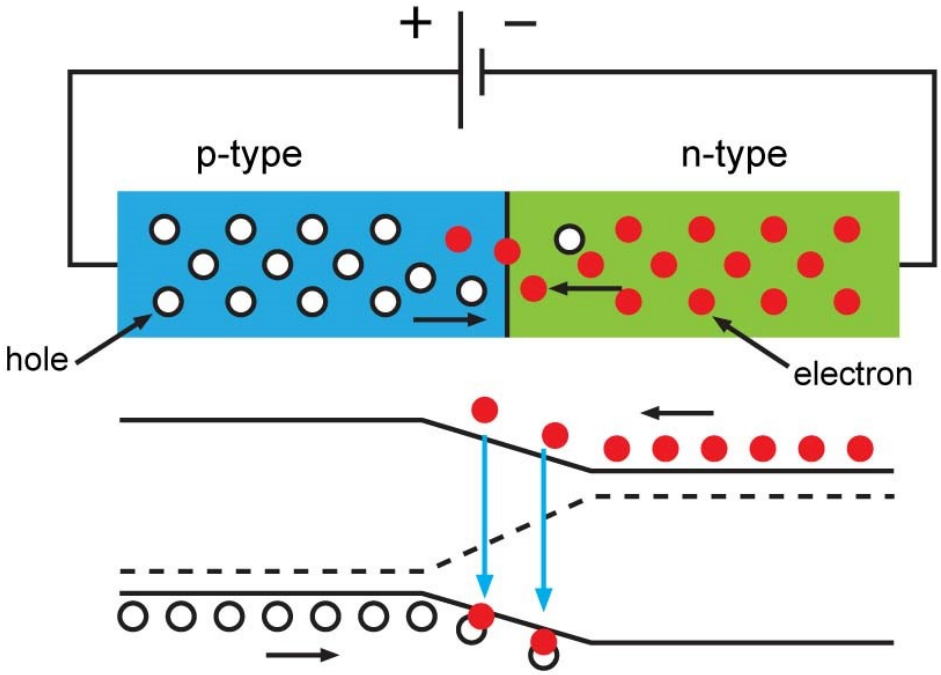

Figure 1.2: A schematic of the circuit in a solar cell, showing p and n type semiconductors in a circuit, electron flow and recombination across the band gap. From http://www.bysolar.com/solar-energy/how-solar-cells-work/ (Accessed January 2017)

from one band to the other without a corresponding change in momentum. As such, the electron must pass through an intermediate process in order to change momentum between the two bands. This behaviour means that indirect band gap semiconductors such as silicon do not absorb light as well as direct band gap semiconductors, where the momentum of the two bands are equivalent and the electron can be excited directly.

Figure 1.3 shows the differences between a direct (left) and an indirect (right) band gap, with the second required step for the indirect band gap semiconductor shown in red.

While first-generation solar cells used silicon, which has an indirect band gap, later-generation solar cells more commonly use semiconductors with direct band gaps, such as CdTe (Cadmium Telluride), CIGS (Copper Indium Gallium Selenide) CZTS (Copper Zinc Tin Sulphide), and MAPI (Methylammonium Lead Iodide $CH_3NH_3PbI_3$) in order to get around this problem.

The ideal band gap for a semiconductor in a solar cell is within the 1.1-1.7

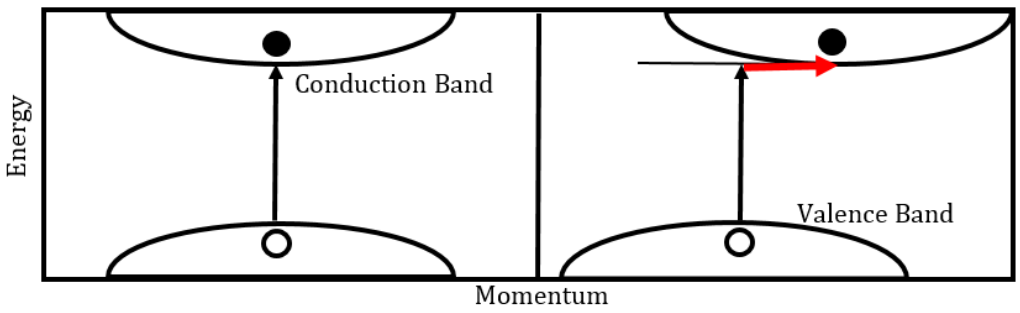

Figure 1.3: A simplified band structure diagram for a direct (left) and an indirect (right) band gap semiconductor. The electrons (black circles) are excited from the valence band to the conduction band, leaving a positively charged electron 'hole' in the valence band. For the indirect band gap semiconductor a second step is needed, as highlighted in red.

eV range, which gives a maximum theoretical efficiency of a single junction cell of ≈34 % according to the Shockley-Queisser limit. The Shockley-Queisser limit is the percentage amount of energy from the sun that can be converted into electricity, with the rest being lost as heat, or from the incident photon passing straight through the cell. Additionally, photons of incorrect wavelength or frequency will be unable to interact with the cell, causing efficiency losses. Figure 1.4 shows the theoretical maximum efficiencies of various common semiconducting materials used in solar cells.

In addition to this, a key requirement for a viable solar cell is the ability to separate the charge carriers into an external circuit without recombining for extended periods of time. This means the material needs to be stable against degradation and against fluctuations in temperature.

1.2 Materials for Solar Cells

Several different semiconducting materials such as silicon and the hybrid perovskite MAPI analogues exhibit these properties, which make them ideal photovoltaics. The most common solar device architectures are centred around crystalline silicon or thin film semiconductors. Common photovoltaics such as dye sensitised, CIGS, CdTe and perovskite-based solar cells can also have thin film architectures.

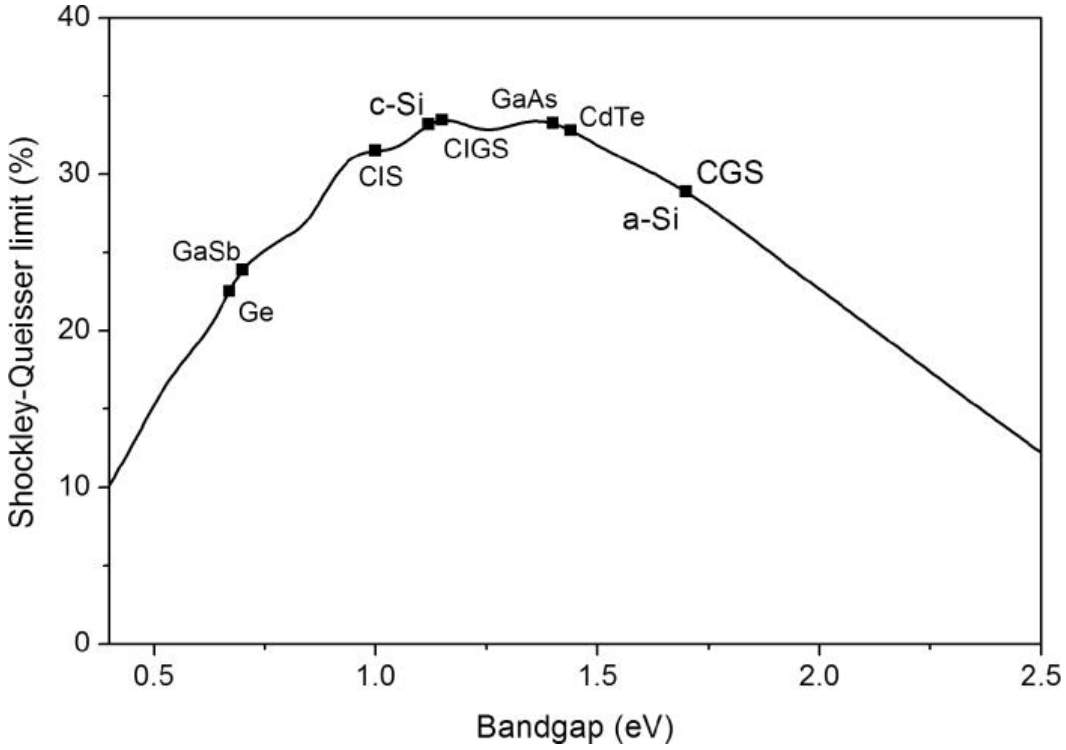

Figure 1.4: The Schockley-Queisser limits of various common solar cell materials, showing the relationship between the band gap of the semiconductor and the theoretical maximum efficiency. The actual efficiency of fabricated solar cells is generally less than the Shockley-Queisser limit. From O. M. ten Kate *et al.*

Globally, a large range of photovoltaic devices have been developed, and can be generally classified into three generations:

1. First generation solar cells are based on crystalline silicon and are the most commonly used commercially.

2. Second generation solar cells are based on thin film technologies and include CdTe and CIGS. These are also used in some commercial applications.

3. Third generation solar cells are new and emerging technologies such as CZTS, organic, and perovskite solar cells. These generally have little commercial application. This project focusses on third generation perovskite solar cells, understanding their properties and improving device efficiency.

In Figure 1.5, the efficiencies of multiple photovoltaic technologies are com-

pared with the best efficiencies reached as of 2016. The first generation of solar cells (purple) are still dominant with efficiencies of up to almost 28 %, while the second generation of cells (blue) have reached efficiencies of 23.3 % and are still rapidly increasing. What is of most interest is the rapid rise in the efficiency of emerging 3rd generation solar cells (orange) within the last 5 years. Already rivalling some second generation cells with rapid rises occurring regularly, it is these which are garnering the most attention in the photovoltaic field.

1.2.1 Silicon and CdTe Solar Cells

The first generation of silicon-based solar cells contained a crystalline silicon semiconducting material, while in subsequent architectures amorphous and semi-crystalline silicon have been used. Crystalline silicon solar cells are the most common production cells with high efficiencies, though are expensive to produce. They were first produced in 1954 by Chapin *et al.*[2] and are the most dominant solar technology on the market, regularly used on roof solar installations. The architecture of the monocrystalline silicon cell centres around a grid of silicon wafers.

The main disadvantage of crystalline silicon solar cells is the relatively small band gap, resulting in a low optical absorption coefficient. This means that silicon needs to be particularly thick to absorb most of the incident light.[3] In order to combat this, the silicon crystal is grown to both high thicknesses and with minimal impurities and defects which may adversely affect the diffusion of charge carriers through the semiconductor.[4] The need for both thick and pure single crystals of silicon is a major contributor to the cost of the technology and later solar cell generations are based upon semiconductors which are both inexpensive and easier to produce. In addition to the small band gap and low optical absorption coefficient, the band gap of silicon is also indirect, contributing to it's electron excitation efficiency.

Second generation CdTe based solar cells are also widely used in solar farms, and are the most common on-silicon based 'thin film' photovoltaic. Compared to silicon solar cells, CdTe cells are both inexpensive, easy to produce, and also have high efficiencies – upwards of 20 %.[5,6] With a near-ideal

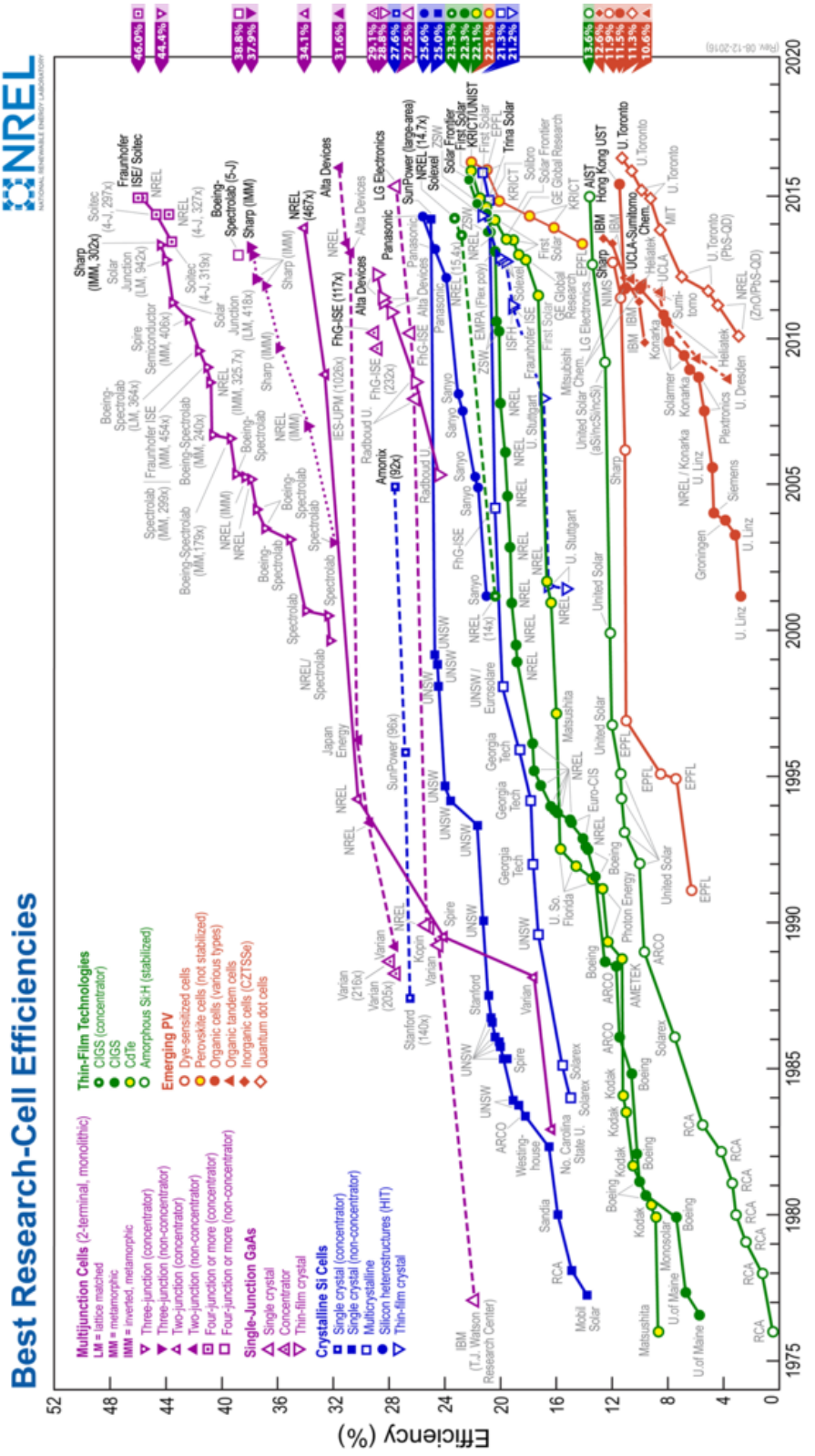

Figure 1.5: NREL research cell efficiencies chart, comparing the evolution of record cells of each type against each other. From the National Renewable Energy Laboratory, http://www.nrel.gov/pv/, (Accessed September 2016)

band gap of ≈1.5 eV the material is therefore able to work with only thin layers, and the material cost of CdTe cells is lower than for silicon. The carrier diffusion properties of CdTe also mean that long diffusion pathways are not needed as compared to monocrystalline silicon. This also results in the production of CdTe cells being more affordable than silicon cells.[4] An additional advantage of CdTe over silicon is the direct nature of the band gap, meaning light absorption is a much more efficient process. It is these properties which cement CdTe as a major competitor with silicon and the second most common semiconducting material used in solar cells after silicon. Conversely, silicon is significantly more abundant than both cadmium and tellurium, which may prove problematic for CdTe cells in the future.

Other second generation solar cells include CIGS and amorphous silicon based cells, which also have some commercial viability but are not as widely used as crystalline silicon and CdTe. CIGS based solar cells are also thin film photovoltaics like CdTe, and have reached similar efficiency levels.

1.2.2 Third Generation Solar Cells

The third generation of solar cells include dye sensitized, CZTS and perovskite solar cells. Known as 'emerging technologies', they do not have any major commercial applications but are the subject of considerable research. Dye sensitized solar cells were the first third generation solar cells to be developed, with efficient cells being produced in 1991.[7] The semiconducting material CZTS is of interest due to having a suitable direct band gap of around 1.5 eV and not containing any toxic material.[8] CZTS solar cell efficiencies have reached upwards of 12 %, cementing their place as potential solar materials but falling far behind other candidate materials such as perovskites.[9] An additional advantage of CZTS is the relative abundance of raw materials in comparison to 2nd generation cells such as CIGS, which contains indium, a metal of low abundance.

First proposed in 2009 and reaching efficiencies of almost 11 % by 2012, the efficiency of perovskite-based solar cells has rapidly passed other third generation technologies such as CZTS and is starting to reach the levels of CdTe and silicon cells.[10,11]

1.3 Lead Halide Perovskites

Over the last few years there have been many new advancements in solar cell technology, brought about by the advent of hybrid organic-inorganic perovskite photovoltaic materials such as methylammonium lead iodide $CH_3NH_3PbI_3$, also known as MAPI. MAPI is currently of interest due to having both good absorption and good semiconducting characteristics. It also has a direct band gap which greatly aids electron excitation.

The potential of these materials is shown in the rapidly increasing efficiencies of the MAPI analogues, rising above 20 %[12] within the space of a few years and beginning to rival other more established technologies. MAPI and it analogues have been shown to be increasingly efficient, but more work is still needed to improve the stability of the cells against degradation in the presence of oxygen, moisture and at high temperatures. Additionally, in some analogous halides the room temperature structure is a non-perovskite, which does not have the same ideal photovoltaic properties. More research needs to be done to determine the stability of high temperature photovoltaic phases.

The fully inorganic perovskite halide $CsPbI_3$ has also shown potential as a solar cell material in its own right, with both the pure iodide and doped iodide-bromide mixed halide perovskites achieving efficiencies close to 10 %[13], with the advantage of being more stable than their mixed organic-inorganic cousins. A disadvantage of the inorganics though is the presence of this non-perovskite phase at room temperature, with the active photovoltaic phase only being stable at higher temperatures.[14] Also, hybrid perovskites have both larger 'A' site cation variability and better thermal stability in fully inorganic systems.[15,16] Of particular concern is the question of how to stabilise this perovskite phase, and whether doping with other halides or tin can lower the phase transition temperature. Further investigation into these systems may garner new insights into both these systems and their hybrid analogues as the search for new photovoltaic materials with increasing efficiencies and stabilities picks up pace.

1.3.1 Perovskite Structure

The structural form of the caesium and mixed organic-inorganic lead halides seen most often in nature is an ideal cubic 'perovskite' structure with space group $Pm-3m$. The perovskite crystal structure has the general formula ABX_3, and is comprised of two cation sites and one anion site. The structure is made up of corner sharing BX_6 octahedra arranged in a cage-like structure around a large central 12-coordinate 'A' site cation. The 'B' site is occupied by a second smaller cation and the 'X' site is occupied usually by a halide or oxide anion. The 'A' site in perovskite oxides is commonly occupied by Ca^{2+}, Sr^{2+}, or Ba^{+}, while the 'B' site is commonly occupied by a transition metal such as Ti^{4+} or Sn^{4+}. In the inorganic perovskite halides studied, the central 'A' site cation is Cs^{+}. In the mixed organic-inorganic perovskite halides, the central cation is typically methylammonium $CH_3NH_3^{+}$, or formamidinium $CH(NH_2)_2^{+}$. The 'B' site in the perovskite halides is commonly occupied by Pb^{2+} or Sn^{2+}. This site arrangement is shown in Figures 1.6 and 1.7.

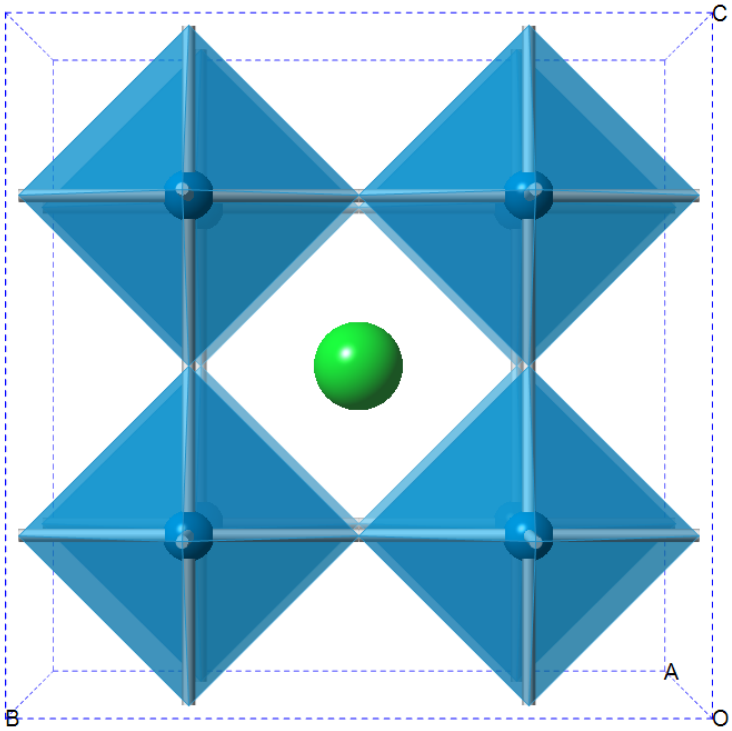

Figure 1.6: The ideal cubic perovskite structure, seen down the (100) plane. Note the corner-sharing BX6 octahedra (blue) surrounding the central 12-coordinate 'A' site (green).

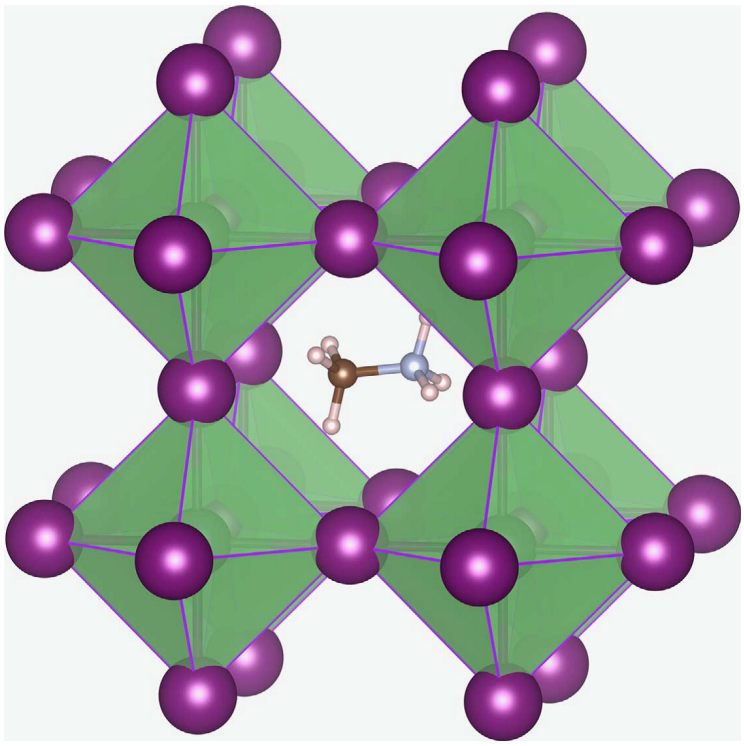

Figure 1.7: Perovskite structure of $CH_3NH_3PbI_3$. Methylammonium cation ($CH_3NH_3^+$) occupies the central A site surrounded by 12 nearest-neighbour iodide ions in corner-sharing PbI_6 octahedra.[17]

The relationship between the three constituent ions, determining whether they form the perovskite structure, is set by the Goldschmidt tolerance factor. A tolerance factor determined from the respective ionic radii of the cations and anion will show whether the ions will form as a perovskite and the level of tilting of the octahedra in the structure. The tolerance factor relationship is shown in Equation 1.1, where r_A, r_B and r_X are the ionic radii of the A, B and X site ions.

$$t = \frac{r_A + r_B}{\sqrt{2}(r_B + r_X)} \tag{1.1}$$

Structures with a tolerance factor (t) of 0.9 – 1 form the ideal cubic perovskite structure, and 0.7 – 0.9 form orthorhombic or tetragonal tilts as the structure shifts to accommodate the smaller 'A' site ions.

As the cation sizes deviate from ideal and the tolerance factor decreases, the BX_6 octahedra tilt to accommodate the ions through the Glazer tilting mechanism.[18,19] The ability of the octahedra to tilt accounts for the large

variability in possible ions that can be incorporated into the perovskite structure, and subsequently the variability in possible constituent ions is what makes perovskite materials so versatile for a large number of different applications. If the 'A' site cation is too small or large for the glazer tilting to accommodate, other non-perovskite crystal morphologies a preferentially formed. $CsPbI_3$ forms the perovskite structure at high temperature, but at room temperature it exists in an orthorhombic 'δ-phase' – also described as the NH_4CdCl_3-structure. Here the corner-sharing octahedra are broken up and instead form edge sharing chains of BX_6 octahedra. Both this structure and the orthorhombic perovskite have the *Pnma* space group and follow the same general formula, but with significant differences in lattice parameters.

In $CH_3NH_3PbI_3$ (MAPI), the 'A' site is occupied by an organic methylammonium ion, with the BX_6 being lead iodide as in $CsPbI_3$. $CH_3NH_3^+$ Is larger than Cs^+, and at room temperature the structure is tetragonal with the PbI_6 octahedra having undergone a tilting away from the ideal cubic symmetry. At high temperature the cubic phase dominates, as shown in Figure 1.7. The related methylammonium tin iodide also is tetragonal at room temperature.[14]

There are multiple MAPI analogues with potential for use in solar cells, with some reaching efficiencies of over 20 %. Table 1.1 lists the efficiencies of a range of inorganic and hybrid perovskite halides such as $CsPbI_3$, MAPI and FAPI, the formamidinium analogue of MAPI.

In FAPI the central cation ($CH(NH_2)_2^+$) is even larger than methylammonium, pushing the room temperature perovskite structure into the ideal cubic symmetry.[30] The variation in possible solar materials shows the tunability of the perovskite structure and the number of possible ways these materials can be manipulated in order to refine the properties of interest. Many of the higher efficiency cells are mixed-cation or mixed-anion perovskites, showcasing the tunability of the perovskite structure and the beneficial effects this can have on device performance.

Table 1.1: Various halide perovskite compositions in order of certified photovoltaic device efficiency.

Structure	Eff %	Year	Reference
$CsPbI_3$	2.9	2015	G. E. Eperon *et al.*[16]
$CsPbIBr_2$	4.7	2016	Q. Ma *et al.*[20]
$FASnI_3$	4.8	2016	S. J. Lee *et al.*[21]
$CsPbBr_3$	5.95	2015	M. Kulbak *et al.*[15]
$CsPbI_2Br$	6.5	2016	R. E. Beal *et al.*[22]
$CsPbI_2Br$	9.8	2016	R. J. Sutton *et al.*[13]
$FAPbI_3$	10.4	2016	C. Yi *et al.*[23]
$MAPbI_{3-x}(SCN)x$	11.07	2015	Y. Chen *et al.*[24]
$MAPbI_3$	15	2013	J. Burschka *et al.*[25]
$Cs_{0.2}FA_{0.8}PbI_3$	15.69	2016	C. Yi *et al.*[23]
$Cs_{0.2}FA_{0.8}PbI_{2.84}Br_{0.16}$	17.35	2016	C. Yi *et al.*[23]
$(FAPbI_3)_{0.85}(MAPbBr_3)_{0.15}$	17.9	2016	J. Seo *et al.*[26]
$(FAPbI_3)_{0.85}(MAPbBr_3)_{0.15}$	18.4	2015	N. J. Jeon *et al.*[27]
$MAPbI_{3-x}Clx$	18.9	2016	J. H. Heo *et al.*[28]
$FAPbI_3$	20.1	2015	W. S. Yang *et al.*[12]
$Cs_{0.1}(MA_{0.17}FA_{0.83})_{0.9}Pb(I_{0.83}Br_{0.17})_3$	21.1	2016	M. Saliba *et al.*[29]

1.3.2 Structural and Physical Properties of Perovskite Iodides

The structural parameters of $CsPbI_3$ are described by Trots and Myagkota[31] along with those of $RbPbI_3$. The room temperature phases of both structures are described as orthorhombic with *Pnma* symmetry, both with the non-perovskite δ-phase orthorhombicity. This δ-phase is lower symmetry than the perovskite phase and has a considerably smaller 'b' lattice parameter than the 'a' parameter, instead of similar values for both, which is usually the case in orthorhombic perovskites. Another major difference between this δ-phase structure and standard orthorhombic perovskite is the rotation of the PbI_6 octahedra. In perovskite structures these are corner sharing, whereas in δ-phase they are edge sharing (Figures 1.8 and 1.9).

At 634 K, $CsPbI_3$ has the cubic perovskite structure whereas $RbPbI_3$ re-

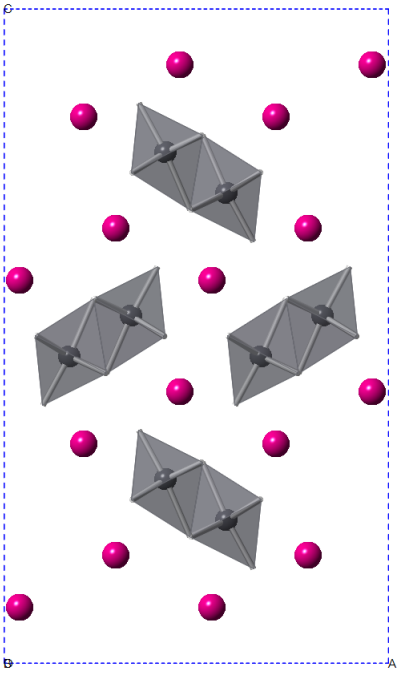

Figure 1.8: The δ-phase orthorhombic structure as seen down the (010) plane. Note the edge sharing PbI_6 octahedra (Grey) surrounded by A site Cs cations (Pink). The cage surrounding the A site is no longer present and there is considerable distortion from the orthorhombic perovskite structure.

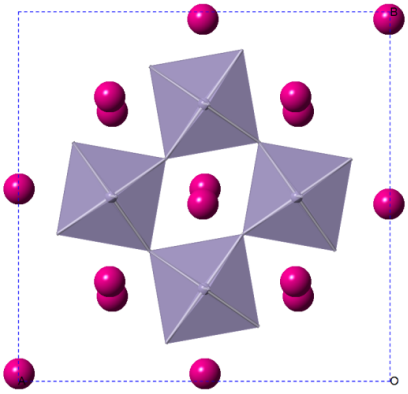

Figure 1.9: The standard orthorhombic perovskite structure as seen down the (001) plane. Note corner sharing octahedra (Grey) surrounding A site Cs cations (Pink). This is a tilted variation of the cubic perovskite structure.

mains orthorhombic. A reversible phase transition from orthorhombic to cubic in $CsPbI_3$ was determined to occur in a two-phase region between 563 K and 602 K, and this was accompanied by a large ($\approx$6.9%) volume change. This phase transition was not found to be present in $RbPbI_3$. $CsPbI_3$ is also characterised by Stoumpos *et al.*[14] alongside the $CH_3NH_3PbI_3$ structure, the

hybrid organic-inorganic perovskite commonly used in perovskite solar cells. The room temperature structure described here is also described as δ-phase orthorhombic in agreement with the Trots structure. These are summarised in Table 1.2

Table 1.2: Experimental structural parameters of various lead halide perovskite compositions at a range of temperatures at 1 atm.

Structure	Lattice parameters / Å			Space group	T / K	Reference
	a	b	c			
$CsPbI_3$	10.458	4.802	17.776	$Pnma$	298	Trots *et al.*[31]
$CsPbI_3$	6.289	6.289	6.289	$Pm-3m$	634	Trots *et al.*[31]
$RbPbI_3$	10.276	4.779	17.393	$Pnma$	298	Trots *et al.*[31]
$RbPbI_3$	10.420	4.841	17.615	$Pnma$	634	Trots *et al.*[31]
$CsPbI_3$	10.434	4.791	17.761	$Pnma$	298	Stoumpos *et al.*[14]
$CH_3NH_3PbI_3$	8.849	8.849	12.642	$I4cm$	293	Stoumpos *et al.*[14]

$CsSnI_3$ has been experimentally characterised by Yamada *et al.* and Chung *et al.*[32,33] Cubic, tetragonal and orthorhombic structures have been characterised, with the cubic phases existing at high temperatures and the orthorhombic phases at room temperature. Yamada *et al.* describe two distinct room temperature polymorphs of $CsSnI_3$, one being the standard orthorhombic perovskite structure and the other the distorted δ-phase. Upon heating, the δ-phase orthorhombic-cubic phase transition occurs at ≈425 K and upon cooling converts to tetragonal at ≈426 K and subsequently to orthorhombic perovskite at ≈351 K.

1.3.3 Structural and Physical Properties of Perovskite Bromides

Rodová *et al.*[34] describe the structure of $CsPbBr_3$ as orthorhombic ($Pbnm$) at room temperature and cubic ($Pm-3m$) at high temperatures, with the transition from orthorhombic to tetragonal being ≈363 K and to cubic being ≈403 K. The nature of the orthorhombic structure is that of a full perovskite instead of the non-perovskite phase of $CsPbI_3$. Stoumpos *et al.*[35] also de-

Table 1.3: Experimental structural parameters of $CsSnI_3$ at different temperatures, showing the cubic, tetragonal and orthorhombic perovskite phases, as well as the orthorhombic non perovskite phase. All structures are at 1 atm.

T / K	Phase	Lattice parameters / Å			Space group	Reference
		a	b	c		
300	Orthorhombic	8.688	12.378	8.643	$Pnma$	Yamada *et al.*[32]
373	Tetragonal	8.772	8.772	6.261	$P4/mbm$	Yamada *et al.*[32]
446	Cubic	6.219	6.219	6.219	$Pm-3m$	Yamada *et al.*[32]
300	Orthorhombic	8.689	12.378	8.638	$Pnma$	Chung *et al.*[33]
300	Non-perovskite	10.350	4.763	17.684	$Pnma$	Chung *et al.*[33]
380	Tetragonal	8.718	8.718	6.1908	$P4/mbm$	Chung *et al.*[33]
500	Cubic	6.206	6.206	6.206	$Pm-3m$	Chung *et al.*[33]

Table 1.4: Experimental structural parameters of $CsPbBr_3$ and $CsSnBr_3$ at room temperature, and high temperature $CsPbBr_3$. All structures are at 1 atm

Structure	Lattice parameters / Å			Space group	T / K	Reference
	a	b	c			
$CsPbBr_3$	8.225	11.759	8.207	$Pnma$	298	Stoumpos *et al.*[35]
$CsPbBr_3$	5.870	5.870	5.870	$Pm-3m$	413	Stoumpos *et al.*[35]
$CsPbBr_3$	5.795	5.795	5.795	$Pm-3m$	298	Somma *et al.*[37]

scribe $CsPbBr_3$ as crystallising in the orthorhombic $Pnma$ space group and undergoing two reversible phase transitions to tetragonal $P4/mbm$ at ≈361 K and to cubic at ≈403 K, which agrees with the Rodová structures. The orthorhombic-tetragonal phase transition is shown to be second order and the tetragonal-cubic phase transition is first order.[35] $CsSnBr_3$, unlike $CsPbBr_3$, is cubic at room temperature.[36]

The optical properties of the $CsPbX_3$ compounds and their relationship to their structures is examined by Somma *et al.* who note the differences between $CsPbBr_3$ and their iodide counterpart.[37] This is explained by the structural differences of $CsPbI_3$ to the bromide, and a lower symmetry Pb^{2+} site. This

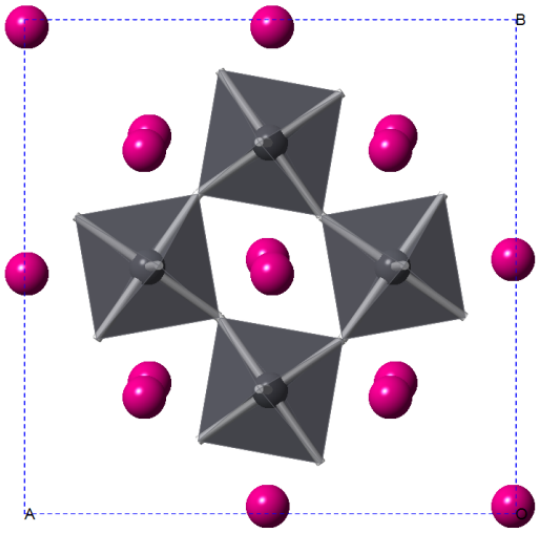

Figure 1.10: The orthorhombic $CsPbBr_3$ structure at 298 K viewed down the (001) plane. Adapted from Rodová et al.[34]

confirms the conclusion of Trots and Myagkota that $CsPbI_3$ crystallises as the HN_4CdCl_3 'δ-phase' orthorhombic structure,[31] and not the perovskite structure of the bromide.

1.3.4 Electronic, Ion Transport and Optical Properties of Perovskite Halides

For their proposed use in photovoltaics, the halide perovskites require both a good band gap in the ideal region and good optical properties. Lang *et al.*[38] calculated the band gaps of $CsPbI_3$, MAPI and their tin halide counterparts. They concluded that the band gap of the material increases with the size of both the 'A' site and 'B' site cations in these structures, and decreases with increasing 'X' anion size. For a semiconductor to have the greatest efficiency in a solar cell the band gap needs to be within the 1.1-1.5 eV range, which four of the structures examined by Lang *et al.* fall within as shown in Figure 1.11, giving them promise as possible photovoltaics.

Chang *et al.*[39] calculated similar band gaps for the methylammonium lead halides to the Lang values, and the trend of decreasing band gap with increasing ionic radius is still present. For both the $MAPbX_3$ structures and the $CsPbX_3$ structures they report values similar to the Lang values but with a smaller range between I and Cl.

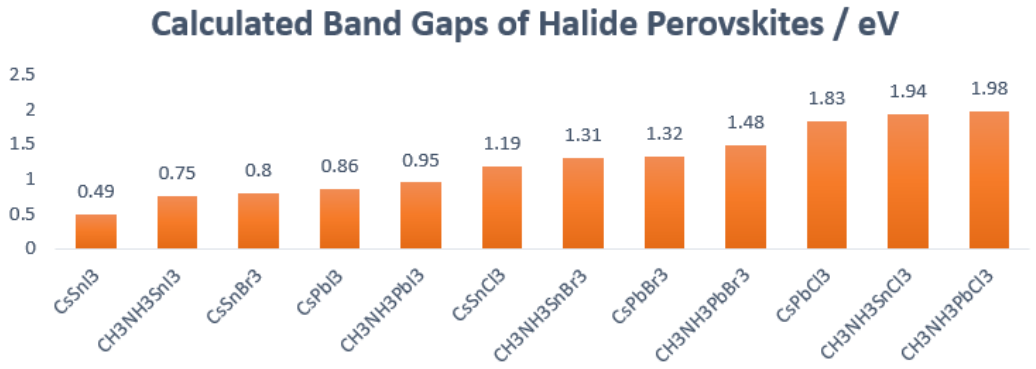

Figure 1.11: Calculated band gaps for a range of inorganic and hybrid halide perovskites. From Lang *et al.*[38]

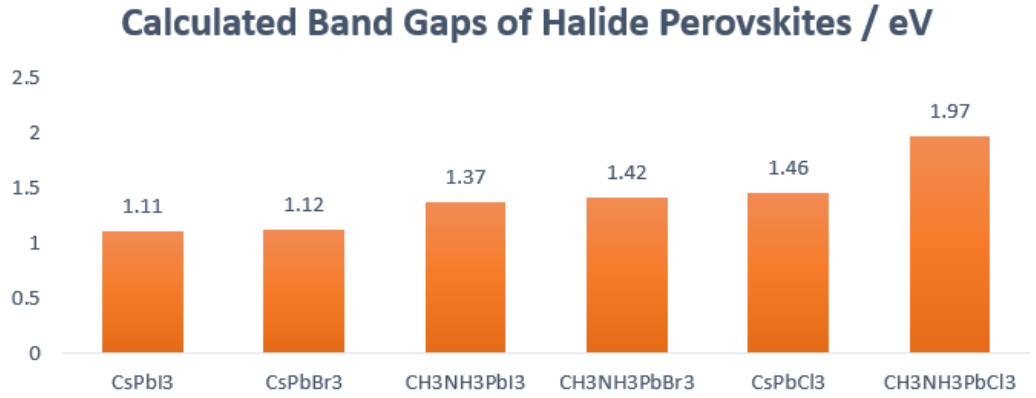

Figure 1.12: Calculated band gaps for a range of inorganic and hybrid halide perovskites. From Chang *et al.*[39]

It is noted that these calculated values are underestimated compared to the experimental values for all structures. For example, for $CsPbCl_3$ the experimental band gap is 3 eV, a difference of 1.54 eV.

Jishi *et al.*[40] compared theoretical and experimental values of band gaps in $CsPbX_3$, $RbPbI_3$ and $MAPbX_3$, (Figure 1.13), calculating theoretical values that are considerably higher than stated in other work but in line with experimental values.

The ionic conductivity of $CsPbX_3$ and related compounds has been studied by Mizusaki *et al.*[41] Mizusaki demonstrated high mobility of halide ion vacancies and low activation energies for both $CsPbCl_3$ and $CsPbBr_3$, and related them to structurally similar $KMnCl_3$. The activation energies obtained

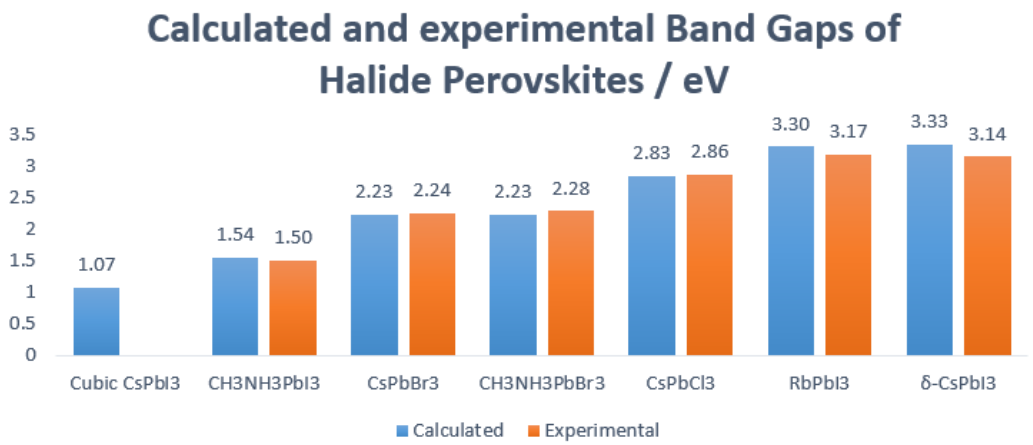

Figure 1.13: Calculated and experimental band gaps for a range of inorganic and hybrid halide perovskites. Calculated values are in blue while experimental values are in red. From Jishi *et al.*[40]

were relatively small in comparison to other ionic compounds.[41] Narayan *et al.* reported similar activation energy values for $CsPbCl_3$ and $CsPbBr_3$, and expanded the investigation to cover $CsCdCl_3$ and $CsSnBr_3$.[42,43] For each of these, the low activation energies demonstrate the facility of ion migration in the materials. For MAPI, Eames *et al.*[17] calculate the I^- activation energy for migration as 0.58 eV, which suggests this is also favourable, and the low activation energies in each of these materials shows promise for use in photovoltaics. For different bromide materials, Kuku *et al.*[44,45] experimentally determined the known activation energies for the perovskite bromides as well as $PbBr_2$. They also describe the conductivities of $CuPbI_3$, $CuSnI_3$ and $KPbI_3$. These values mostly agree with the other literature data, and as such there is a relatively clear picture of the expected energy values for most materials with the perovskite structure and this set of ions.

A recent DFT study on the iodides and bromides also places the ion migration values in this region, with an I^- migration value of 0.36 eV or 0.29 eV depending on the migration pathway.[46] This fits with the trend seen in $CsPbBr_3$ and $CsPbCl_3$. The $MAPbI_3$ value recorded is lower than the Eames (2015) value – 0.28 eV compared to 0.58 eV, but both papers show I^- migration having a lower activation energy than MA^+ or Pb^{2+} migration.[17,46] Optically, $CsPbBr_3$ and $CsPbCl_3$ exhibit similar properties whereas $CsPbI_3$ is markedly different. The $CsPbI_3$ emission spectra has a broad band at 535 nm,

Table 1.5: Activation energies for halide ion migration in various halide perovskite compositions, from Mizusaki *et al.*, Narayan *et al.* and Eames *et al.*[17,41–43]

Structure	E_a / eV
$CsPbBr_3$	0.29
$CsPbCl_3$	0.25
$KMnCl_3$	0.39
$CsCdCl_3$	0.86
$CsSnBr_3$	0.15
$CH_3NH_3PbI_3$	0.58

Table 1.6: Activation energies for halide ion migration in various halide perovskite compositions from Kuku *et al.*[44,45]

Structure	E_a / eV
$CsPbBr_3$	0.25
$CsSnBr_3$	0.34
$CuPbBr_3$	0.27
$PbBr_2$	0.23
$CuPbI_3$	0.26
$CuSnI_3$	0.29
$KPbI_3$	0.32

whereas the other materials are characterised by narrower peaks and apparent shorter decay times in the nanosecond range compared to microsecond times for $CsPbI_3$.[37] This can be attributed to lower symmetry Pb^{2+} sites present in $CsPbI_3$ and subsequent Jahn-Teller distortion of the Pb^{2+} excited state and self-trapping of excitons. In the emission spectrum of $CsPbBr_3$ both trapped and free exciton emissions are present, with very short decay times for the free excitons. There is a broad emission at 535 nm as in $CsPbI_3$ and a free exciton line at 533 nm.

Absorption spectra of $CsPbBr_3$ suggest that the material is a direct band gap semiconductor in both the room temperature and high temperature phases of the material.[47] $CsPbCl_3$ is also known to be particularly luminescent, the luminescence spectrum of which has three bands, the highest energy of which is attributed to free excitons and the others to trapped excitons. This pattern also exists in the $CsPbBr_3$ luminescence spectrum.[47–49] At least three emission processes are present in $CsPbCl_3$ luminescence – free Pb^{2+} cation exciton emission, bound exciton emission and emission from Pb^{2+} trap states. The energy of each decreases in the order free – bound – trapped. Efficient energy transfer in $CsPbCl_3$ takes place between the free and bound excitons.[50]

1.3.5 Mixed 'A' Site Cation Perovskite Halides

As shown in Table 1.1, the perovskites with the highest efficiencies are $CH(CH_2)_2PbI_3$ (FAPI) and the mixed 'A' site cation compositions with FAPI as a base material. The archetypal MAPI is thermodynamically unstable[51–53] and compositions with a different 'A' site cations have been seen to improve both the stability and photovoltaic performance.[23,27,29,54–58]

These mixed cation systems usually consist of a FAPI host phase which is then doped with small quantities of MA^+, Cs^+ and Rb^+ onto the 'A' site. This doping improves the performance via three suggested mechanisms:

1. Lowering of the Gibbs free energy due to the entropy of mixing.[23,59]
2. Lowering the Goldshmidt tolerance factor due to the tilting of the octahedra on doping with smaller cations.[60,61]
3. Reducing the strain in the crystal through strain-relieving relaxation.[62]

At room temperature, pure FAPI has a non-perovskite 'yellow phase' structure as with $CsPbI_3$, with the material also having a higher temperature cubic perovskite phase.[14,30] It is this cubic perovskite phase that is used as the base for our investigation. The phase behaviour of MAPI-FAPI solid solutions has already been studied in detail,[56] and in this project we aim to understand why there is an increase in phase stability as a result of these mechanisms. Doping with Cs^+ and Rb^+ will be used as archetypal systems due to the size imbalance between the cations and FA^+.

1.4 Aims of the Project

In this project, computer modelling techniques based on both interatomic potentials and *ab initio* methods will be used to understand the properties of halide perovskite materials for use in solar cells. Two primary objectives are identified:

1. To develop an interatomic potential model which accurately reproduces all the known experimental structures of the $Cs(Pb,Sn)(I,Br,Cl)_3$ series. This has not been achieved before for this system and is particularly challenging due to both the varying levels of covalency and the change in structures between the perovskite and non-perovskite phases.

   This model can then be used to investigate the effect of varying the 'A', 'B' and 'X' ions in the perovskite structure. It has been shown that mixed 'A' and 'X' site halides have considerable promise as photovoltaics, so investigating how the structure changes and adapts on doping is of great interest. The primary focus of this objective will be on 'A' site doping in $CsPbI_3$, and how this affects the phase stability of the perovskite and non-perovskite phases of $CsPbI_3$. This is of particular importance as the non-perovskite room temperature phase of $CsPbI_3$ is not photoactive.

2. To understand how varying cation doping on the 'A' site in FAPI affects the physical properties of the material. This is key in understanding how the efficiency of perovskite solar cells varies on 'A' site cation doping. Phenomena such as the tilting of the PbI_6 octahedra and octahedral locking are investigated to understand how these affect the structure of

the material and properties such as the band gap. This is probed using *ab initio* molecular dynamics.

A general goal of this work will be to use the information gathered to inform experiment and to further explore the viability of the perovskite halides as materials for use in solar cells.

Chapter 2

Methodology

"It is a mistake to think you can solve any major problems just with potatoes"

Douglas Adams
Life, the Universe and Everything

In order to examine the properties of materials at atomic level, a number of computer modelling techniques have been developed, and have proved themselves to be both powerful and accurate tools. The use of computational modelling means that the intrinsic structural properties of a material may be examined on a very small scale and without the need for lab based analytical techniques. The fundamental basis behind computational modelling is deriving the level of interaction between each atom in a studied system, and the potential energy of a system is then determined as a function of these interactions. Computational simulation can then be used to explore the potential energy landscape of a system and can probe effects such as defect incorporation in a crystal or can be used to determine the lowest energy configuration of a structure. This computational model of a system can be generated either from experimental data such as XRD patterns, or from *ab initio* methods, with the model being refined so it accurately fits any experimental data on the given system.

A general overview of the computational techniques used in this study is presented here, with the techniques described in more detail elsewhere.[63,64]

2.1 The Potential Model

The potential model in computational chemistry describes the energy of a system as a function of its coordinates, and in a pair potential between two atoms as a function of the interatomic separation. In atomistic simulation these potentials account for the interactions between all the atoms in a crystal, for example in a system comprised of atoms A and B, there would be A-A, A-B and B-B pair potentials. The total energy of a system would then be the sum of these interactions. Use of pair potentials has become widespread in the computational chemistry community for their ability to accurately calculate structural properties of crystalline materials.[65–68]

A pair potential generally comprises both short range and electrostatic (longer range) interactions between two atoms, fit to a potential equation such as the Buckingham, Lennard-Jones, and Morse potential forms. This reflects the interactions between atoms in a crystal, where there are both attractive forces pulling the atoms together and repulsive forces pushing them apart. Common attractive forces within a crystal are Coulombic and Van der Waals interactions, while repulsion between the electron clouds of the atoms are common repulsive forces. At a certain distance either the attractive or repulsive interaction will be dominating, which the potential then maps. These common potential forms are summarised in Table 2.1 and an example potential is presented in Figure 2.1, outlining both the attractive and repulsive contributions to the final potential.

The Buckingham potential describes the interactions between two specified atoms as a function of their interatomic distance r, and is comprised of three variable parameters – A, ρ, and C, which constitute both an attractive and repulsive component. The repulsive and attractive components of the Buckingham potential are $A\ exp(\frac{-r}{\rho})$ and $\frac{C}{r^6}$ respectively. The full Buckingham potential includes a Coulombic term, further describing the charged interactions between two ions, where the q_1 and q_2 terms are the charges of the ions. This gives the potential the form shown in Equation 2.1:

$$\Phi(r) = Aexp(\frac{-r}{\rho}) - \frac{C}{r^6} + \frac{q_1 q_2}{4\pi\epsilon_0 r} \tag{2.1}$$

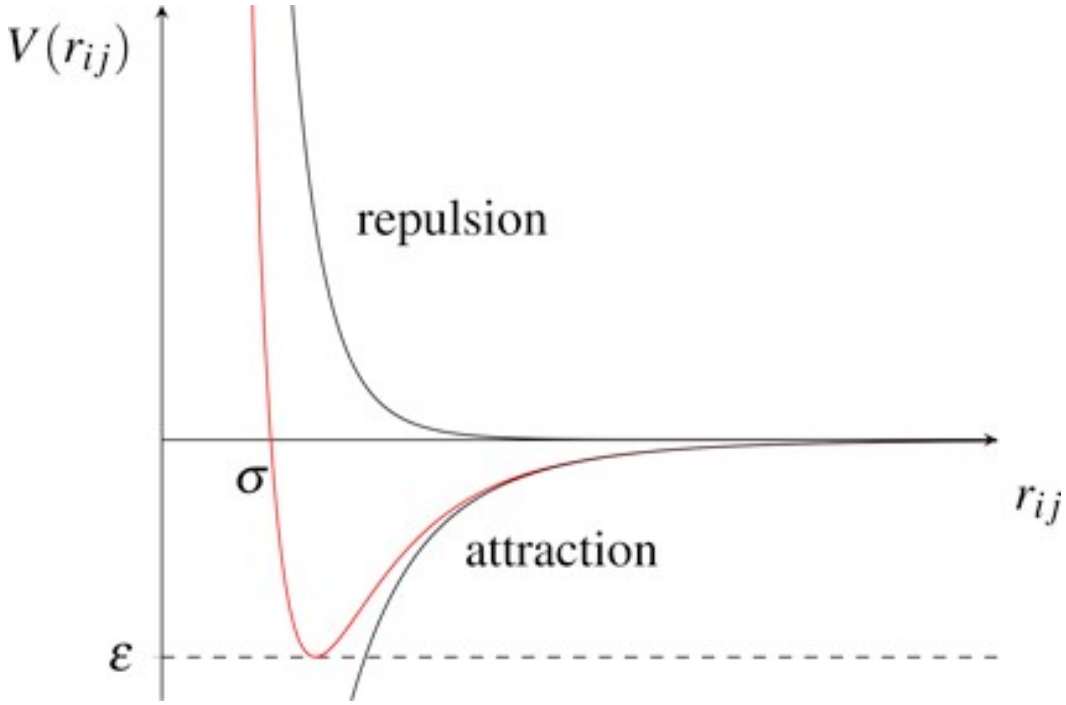

Figure 2.1: An example interatomic potential between atoms i and j, showing both the attractive and repulsive contributions to the final potential (red),where $V(r_{\mathrm{ij}})$ is the potential energy and r_{ij} is the interatomic separation between the two atoms. ϵ and σ are the depth of the potential well and the position where the potential is zero. From *Computational Approaches in Physics*, 2016[69]

The Morse potential is formed in a similar manner to the Buckingham, with both a long range attractive and a short range repulsive part. The variable parameters of the Morse potential are D, a and r_0. Here D is the bond/well depth, a is the potential well width, and r_0 is the equilibrium bond length, the location of the bottom of the well.

Table 2.1: Common interatomic potential forms used in computational modelling.

Potential Name	Functional Form
Buckingham	$\Phi(r) = Aexp(\frac{-r}{\rho}) - \frac{C}{r^6} + \frac{q_1 q_2}{4\pi\epsilon_0 r}$
Lennard-Jones	$V_{\mathrm{LJ}} = 4\epsilon[(\frac{\sigma}{r})^{12} - (\frac{\sigma}{r})^6]$
Morse	$V(r) = D_{\mathrm{e}}[(1 - exp(-a(r - r_0)))^2 - 1]$

In this investigation a Morse potential was fit to the investigated structures, though as each potential form describes the same interaction they can

be used interchangeably.

In addition to the potential forms specified above, there are also constraints which can be added in order to further describe the interatomic interactions such as the utilisation of the shell model.

2.2 The Shell Model

An additional layer of theory used to describe the interactions between atoms in a crystal is the shell model. Developed by Dick and Overhauser in 1958,[70] the shell model is used to describe additional effects such as polarisability on the atoms in the simulation. Essentially, the shell model splits the simulated atom into an inner 'core' and an outer 'shell'. The core consists of the nucleus and inner electrons, while the shell primarily consists of the valence electrons. Between the rigid, immovable core and the outer shell is a harmonic spring of rigidity (spring constant) k. As k increases, the polarisability of the ion decreases and the rigidity of the spring increases, meaning the shell cannot move as far from the initial atomic position once a force has been applied to it. As such this spring constant is directly related to the polarisability of the ion in a vacuum (α), as shown in Equation 2.2:

$$\alpha = \frac{q_s^2}{k_{\mathrm{cs}}} \tag{2.2}$$

The force constant k_{cs} is the spring constant, and is related to the polarisability through the shell charge q_s. The sum of the shell and core charges is the oxidation state of the ion. As the potential is applied to the atom, a dipole moment is produced as the shell moves away from the core to a certain distance depending on the level of polarisability.

2.3 Energy Minimisation

The essential first step in solving a computational problem is the energy minimisation. Energy minimisation relaxes the ions in a structure into their most stable configuration. Once a structure has been minimised then subsequent computational experiments can be undertaken and specific atomic properties can then be studied and predicted.

There are multiple possible energy minimisation techniques which can be employed to find an energy minimum. An energy minimum is the point on an energy surface where the energy of the system is lowest, with the energy surface being defined as a multidimensional 'map' of all the possible configurations of the material and their related energy level. Some techniques analyse the gradient of the surface and proceed down the steepest slope to a minimum, whereas other techniques such as particle swarm optimisation can use more complex analyses to determine better routes to possible energy minima. Any general minima on the energy landscape are 'local' minima, while the lowest energy minimum is the 'global' minimum. The global minimum on the energy landscape for a crystal structure is the most thermodynamically stable configuration of the atoms. Optimisation techniques which focus solely on reaching the bottom of an energy well the system is in are defined as local optimisation techniques, whereas techniques which can more easily explore larger parts of the potential energy surface are defined as global optimisation techniques.

Generally, the global minimum is required and as such global techniques may be better, but they are also computationally more expensive and take significantly longer than most local techniques. As such, it is sometimes preferred to start the optimisation at a position on the energy surface known to be close to the global minimum and use a local technique to find it rather than always using global optimisation methods. This is usually achieved by starting the optimisation run from experimental data, or shrinking the energy surface by eliminating unphysical values.

2.3.1 Local Optimisation Methods

The main optimisation code used in this study is the General Utility Lattice Programme (GULP)[71,72]. Within GULP, common local minimisation methods utilised are steepest descent, conjugate gradient and Newton-Raphson optimisation, with steepest descent being the most basic. Each of these optimisation methods involves an energy calculation at a defined 'step', with each step having a slightly different geometry and the method of reaching each step differing depending on the optimisation method. With each step the algorithm aims to head towards the required minimum.

A steepest descent algorithm searches the energy landscape to find the line of steepest gradient from the starting point of the simulation. At each iteration i, the gradient is determined and the updated search direction r_i is defined by taking the negative of the gradient, as shown in Equation 2.3:

$$r_\mathrm{i} = -g_\mathrm{i} \tag{2.3}$$

The algorithm then proceeds along this direction towards the next step. This algorithm can rapidly head downhill towards a minimum but is very dependent on both step size and starting point location. If the step size is too large then the algorithm may overshoot the minimum or miss it completely. As such, this method is a lot more preferred for the initial steps in the simulation far from the minimum, and methods such as Newton-Raphson which can more efficiently map the minimum preferred for the later steps in an optimisation. Equation 2.4 shows how the atomic configuration is updated during each step:

$$x_{\mathrm{i}+1} = x_\mathrm{i} + \alpha_\mathrm{i} r_\mathrm{i} \tag{2.4}$$

Where x_i is the initial configuration, $\alpha_\mathrm{i} r_\mathrm{i}$ is a step of arbitrary length α_i along the direction r_i and $x_{\mathrm{i}+1}$ is the updated configuration.

Conjugate gradient optimisation is similar to steepest descent, but while steepest descent minimises the energy along a series of orthogonal lines, conjugate gradient takes a whole set of orthogonal search vectors d_n and only minimises the energy once. The configuration is then updated using Equation 2.5:

$$x_{\mathrm{i}+1} = x_\mathrm{i} + \alpha_\mathrm{i} d_\mathrm{i} \tag{2.5}$$

Where d_i is the updated search vector.

Newton-Raphson optimisation analyses the curvature of the energy surface within the optimisation algorithm, and this additional information leads to a more 'direct' route towards the minimum being taken. This means Newton-Raphson is more accurate than other techniques, but additional computational time is required for each step, as the second derivative of the function (the Hessian matrix) is also evaluated, which determines the curvature of the

energy surface. Therefore it is common to use both methods in succession, initially employing steepest descent then switching to Newton-Raphson at a user-defined point.

Newton-Raphson works by including the gradient, which is the first derivative of the function, and the Hessian matrix in each step. Previous methods include the gradient but do not take into account the Hessian matrix. It is this additional parameter which increases the accuracy of the optimiser, but also significantly increases the time taken to perform an optimisation. The atomic configuration is updated on each step in accordance with Equation 2.6 where H_{i} is the Hessian matrix and g_{i} is the gradient at each step.

$$x_{\mathrm{i+1}} = x_{\mathrm{i}} - H_i^{-1} g_{\mathrm{i}} \tag{2.6}$$

2.3.2 Global Optimisation Methods

Global optimisation, as opposed to local optimisation, tends to explore the entire energy landscape, or a large predefined area of it, instead of just the area within a single minimum. Generally taking significantly longer and using a lot more computational power, they greatly improve the chance of the final structure being the global energy minimum, but at considerable overhead cost.

In this investigation, two different global optimisers have been utilised, with particle swarm and evolutionary algorithms being used for refining the potential model.

2.3.3 Particle Swarm Optimisation

The 'particle swarm' optimisation method is one of the most versatile methods that can be used for optimisation of complex problems. Unlike standard optimisers which analyse the goodness of fit at a particular point on the energy landscape, the particle swarm uses a series of points (particles) concurrently, and thus can analyse a wide search space. Each particle is a separate arrangement of atoms or values and is a theoretical result of the optimisation calculation like any step in a local optimisation algorithm. In practice, the 'swarm' of particles moves across the defined search space with positions and velocities influenced by the goodness of fit of the entire set.

A given population size of particles are initially distributed randomly on the energy landscape, independently generating a 'sum of squares' – an indication of how far away the particle is from the global minimum. The difference between the physical properties of the ideal structure and the structure at the point the algorithm has reached are squared and multiplied by a weighting function, with larger values being further from the ideal structure. Each particle in the swarm then communicates this sum of squares with the rest of the swarm, with the values being compared and a global best known position is identified where the sum of squares is lowest.

On knowledge of the global best position, the individual particles start moving towards that position in a series of iterative steps. The distance 'travelled' by the particle in each step is determined by the proximity to the global best fit in the search space – particles further from the minimum are given larger velocities and travel in larger jumps at each step. After each subsequent iteration, the global minimum position is updated and the velocities and directions of the particles updated to account for this. Eventually the set of particles will converge near the minimum position, narrowing in on a small search area from the wider search. Through this the global minimum should be found, though there is still propensity for the swarm to fall into a local energy well. The speed and efficiency of the particle swarm algorithm are linked to the initial number of particles – the population size – with more particles being able to more efficiently scan an area, but taking longer to do so.

2.3.4 Evolutionary Optimisation

An alternative optimisation method which is less likely to fall into a local minimum is the evolutionary (genetic) algorithm. This works in a similar way to the particle swarm, though there is a propensity for large jumps across the search space in each step which may eliminate the problem of becoming stuck in local minima.

The principle behind the evolutionary algorithm is based on the principles behind Darwinian evolution, with a set of species which 'evolves' through a series of 'mutations' over time with more ideal mutations being favoured

until the most ideal result is found. Based on genes in cells, each individual 'chromosome', analogous to the particles in a particle swarm, contains a string of information which upon each iteration of the code can divide and recombine to form 'offspring' in the form of new chromosomes. Offspring with more favoured information are preferred, eventually meaning an ideal chromosome is formed at the minimum.

The genetic algorithm is a global optimisation method like particle swarm, but with a greater possibility of not getting stuck in local minima due to the random chance of 'mutations' occurring in each gene at each step. These mutations can cause the location of the chromosome on the energy surface to jump over barriers that previously would not have been passable due to unfavourable energetics. The initial population size, as with in particle swarm optimisation, determines the speed and efficiency of the search space exploration. Too few chromosomes in the population means only a small search space is explored whereas too many chromosomes means the algorithm, though able to search large amounts of information, will take a very long time to complete.

2.4 Defect Simulation

Within a crystal lattice, there are two types of intrinsic stoichiometric defects which always form in a structure above absolute zero. These defects are charge neutral and therefore retain the overall neutrality of the crystal. This is achieved by the movement of stoichiometric units of atoms within the lattice, either through vacancy formation or interstitial formation.

1. Schottky Defect: The Schottky defect is where stoichiometric units of the crystal are removed from the bulk to the surface. This can either be a small charge balanced unit such as CsI or PbI_2, or can be a full unit: $CsPbI_3$.

2. Frenkel Defect: The Frenkel defect is where an ion is moved from a lattice point to an interstitial point elsewhere in the bulk of the crystal. This creation of both a vacancy and an interstitial means charge balance is retained.

In computational simulations, these stoichiometric defects can be modelled by creating point defects – vacancies and interstitials – in the bulk lattice. Their formation energies can then be examined. A third type, the substitutional defect, can also be modelled by replacing an atom on a lattice site with an impurity.

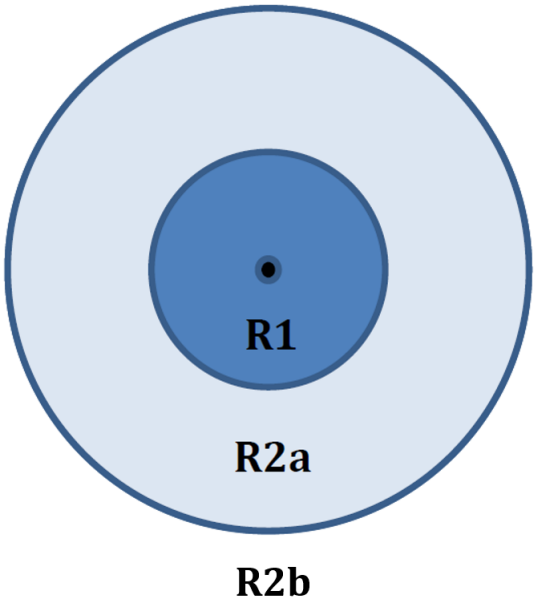

Figure 2.2: Inner sphere and outer sphere of a Mott-Littleton cluster. The defect centre (black) is surrounded by a sphere of ions explicitly affected by the defect (dark blue) named region 1, which is in turn surrounded by a sphere of ions where the effect of the defect is approximated (light blue), region 2a. Region 2b surrounds these regions and extends to infinity.

Simulating these defects in crystals is generally achieved by the 'Mott-Littleton' method. The Mott-Littleton method, first developed in 1938 by N. F. Mott and M. J. Littleton[73], defines spherical regions around a central point called the 'defect centre' and uses these regions as a guide for relaxation of the crystal. Region 1, the inner sphere, contains ions which are strongly affected by the defect and therefore are all allowed to relax round the centre and move freely. The outer spheres, called regions 2a and 2b, contain ions that are only weakly affected by the defect. The energies of the ions in region 2a are only approximated instead of being explicitly calculated, with the region 2b energies being neither calculated or approximated. This region extends to infinity in every direction. The sum of the energies of each region is the total

energy of the defect or defect cluster. Figure 2.2 shows the makeup of these regions within the cluster.

2.5 Molecular Dynamics

The disadvantage of energy minimisation is the inability of the methods to offer any information as to the kinetics of the studied systems, due to all the simulations being performed at absolute zero. Though giving large amounts of information about a studied system, any thermal effects are ignored. Molecular dynamics (MD) counters this by explicitly including the kinetic energy of the calculated system. The MD codes used in this investigation are LAMMPS and CP2K.[74,75]

This additional kinetic factor means MD simulations can overcome local energy barriers and travel uphill on the potential energy surface, therefore being able to explore minima which would previously not be able to be considered with standard energy minimisation.

Within MD, each atom is assigned a velocity, which then directly relates to the temperature of a system. The positions and velocities of these atoms are then measured over time using Newton's laws of motion. The second law of motion (Equation 2.7) relates the mass and acceleration of an object to the force acting upon it, and therefore by knowing the velocity and position of each atom at a certain moment in the simulation all the forces can then be known.

$$f = ma \tag{2.7}$$

An MD simulation proceeds by solving this equation along a series of iterative moments, or timesteps, where after each timestep (Δt) the values of velocity (v_i) and iteration (x_i) are iteratively updated. The value of acceleration is then determined from the force as derived from Equation 2.7 and combined with the velocity at time t to generate an updated velocity at $t + \Delta t$. Equations 2.8 and 2.9 show the method through which this is calculated.

$$v_\mathrm{i}(t + \Delta t) = v_\mathrm{i}(t) + a(t)\Delta t \tag{2.8}$$

$$x_{\mathrm{i}}(t + \Delta t) = x_{\mathrm{i}}(t) + v_{\mathrm{i}}(t)\Delta t \tag{2.9}$$

The value of the timestep is chosen dependent on the system and is usually on the femtosecond scale, as this is the timescale in which forces acting on an ion are most accurate.

2.5.1 The Timestep and Equilibration

A major consideration when running MD simulations is the choice of the timestep (Δt). The value chosen must be smaller than the timescale of any of the processes by the simulation, otherwise the effect of the process will be missed by the simulation. Additionally a small timestep is more accurate than a large timestep, with the caveat that a smaller timestep means the simulation requires more computational time to compute.

If too large a timestep is chosen, the simulated ions can move unphysically and have an excessively large amount of energy, destabilising the system. Therefore to get the right balance between fast calculation and accurate calculation a lot of trialling is usually needed. This balance usually comes between the 0.1 and 1 femtosecond timestep, which is large enough to study a large amount of simulation time quickly while still being accurate. This timestep and the overall simulation time depends on the property being studied, with long processes such as diffusion needing longer timescales and timesteps and processes such as electron relaxation occurring much faster and needing shorter timesteps.

Once an appropriate timestep is chosen the simulation is set in motion, with the objective being to cover a large enough amount of simulation time to study the desired properties in their entirety. This can be in the scale of picoseconds or nanoseconds. Initially the simulation needs to undergo an equilibration period, where the system relaxes from it's initial static structure into equilibrium. This equilibrium is achieved when the total energy of the system has settled down into a steady minimum and the properties of the system have converged to a satisfactory degree.

After equilibrium has been reached, the simulation is then set to continue to run until a satisfactory amount of time has passed dependent on the data

being collected, normally on the picosecond or nanosecond scale. It is during this phase that the desired results of the simulation are collected.

Both potentials-based MD, which utilises interatomic potentials to measure the interactions between ions, and *ab inito* MD where the energy of the system is explicitly calculated from theory, work in a similar manner, with the main difference being the creation of the initial model. Additionally potentials-based MD calculates everything classically whereas *ab inito* MD introduces quantum effects. Potentials-based methods are derived mainly from experimental data, whereas *ab initio* methods are derived from solving the Schrödinger equation for the system in each step. This builds on Density Functional Theory, which is examined in more detail below.

2.6 Density Functional Theory

While interatomic potentials-based models are based upon using experimental data to reproduce experimental characteristics of a real system, Density Functional Theory (DFT) is an *ab initio* technique which calculates the characteristics of a system directly from theory. This allows insight into the ground-state properties of a material which empirical methods would be unable to provide, such as charge distribution and band structure. These *ab initio* quantum mechanical techniques aim to generate this information by solving the Schrödinger equation and subsequently deriving the exact wavefunction of the modelled system. The simplest form of the time-independent Schrödinger is shown in Equation 2.10, where $\hat{H}$ is the Hamiltonian, ψ is the wavefunction and E is the total energy of the system.

$$\hat{H}\psi = E\psi \tag{2.10}$$

Within the wavefunction all the information regarding the positions and spins of the particles within the system are contained, and from this all material properties of a system can then be calculated. The eigenvalue of the Hamiltonian operator equals the total energy of the system, and therefore an appropriate solution to the Schrödinger equation can be found by identifying an appropriate form of the Hamiltonian.

The full Hamiltonian is shown in Equation 2.11, Where $\hat{T}_{\mathrm{e}}$ is the electronic

kinetic energy, $\hat{T}_{\mathrm{n}}$ is the nuclear binding energy, and the $\hat{V}$ terms make up the potential energy of the system. $\hat{V}_{\mathrm{int}}$ describes the electron-electron interactions, $\hat{V}_{\mathrm{nn}}$ describes nuclear-nuclear interactions and $\hat{V}_{\mathrm{ext}}$ describes the electron-nuclei interactions.

$$\hat{H} = \hat{T}_{\mathrm{e}} + \hat{T}_{\mathrm{n}} + \hat{V}_{\mathrm{int}} + \hat{V}_{\mathrm{nn}} + \hat{V}_{\mathrm{ext}} \tag{2.11}$$

A complete description of the studied system can then be provided by summing these terms over the masses and positions of all the nuclei and electrons in the system, as described in Equation 2.12. The mass and position of nucleus I are defined by $\mathrm{M_I}$ and $\mathrm{R_I}$, with the charge defined by $\mathrm{Z_I}$. The mass and position of electron i are defined by $\mathrm{m_e}$ and $\mathrm{r_i}$.

$$\hat{H} = \frac{-h^2}{2m_{\mathrm{e}}} \sum_i {\nabla_{\mathrm{i}}}^2 - \sum_I \frac{h^2}{2M_{\mathrm{I}}} {\nabla_{\mathrm{I}}}^2 + \frac{1}{2} \sum_{i \neq j} \frac{e^2}{|r_{\mathrm{i}} - r_{\mathrm{j}}|} + \frac{1}{2} \sum_{\mathrm{I} \neq \mathrm{J}} \frac{Z_{\mathrm{I}} Z_{\mathrm{J}}.e^2}{|R_I - R_J|} - \sum_{i,I} \frac{Z_{\mathrm{I.e}}}{|r_{\mathrm{I}} - R_{\mathrm{I}}|} \tag{2.12}$$

This problem cannot be solved exactly for many-body systems with multiple electrons, and a series of approximations need to be used in order for the problem to be solved using current computational methods. The Hohenberg-Kohn theorems are one method to simplify the problem, and form the basis of modern Density Functional Theory.

1. The three dimensional electron density of a many electron system uniquely determines all the ground state properties of the system.

2. The energy of a system can be defined as a functional of the electron density, with the minimum energy functional corresponding to the ground-state electron density.

As a result of the first theorem, the solution of the multiple electron wavefunction is no longer required, and instead the three-dimensional electron density $\rho(r)$ is all that is needed to understand the studied system. The result of the second theorem is that the ground state electron density can be calculated by defining the energy functional of the system, and the ground state electron density can then be used to define all the other properties of the studied system. The resultant energy functional of the system is described in Equation 2.13.

$$E[\rho(r)] = \int V_{ext}(r)\rho(r)dr + F[\rho(r)] \tag{2.13}$$

with $\int V_{ext}(r)\rho(r)d(r)$ describing the interactions between the electrons and the external potential, while $F[\rho(r)]$ describes the kinetic information of the electrons in the system and the electron-electron interactions. These theorems provide the basis for DFT and remove a lot of the complexity of the problem. The Kohn-Sham equations have then built upon this to solve the form of $F[\rho(r)]$, which is still unknown. Equation 2.14 splits the unknown term into several terms which can then be solved exactly.

$$F[\rho(r)] = E_{ke}[\rho(r)] + E_H[\rho(r)] + E_{xc}[\rho(r)] \tag{2.14}$$

Where the kinetic energy of the non-interacting electrons is described by $E_{ke}[\rho(r)]$, and the Hartree term $E_H[\rho(r)]$ describes the Coulombic energy of the electron-electron interactions. The final term $E_{xc}[\rho(r)]$ describes the contribution to the energy from the exchange correlation function and the energy difference between the real and hypothetical systems. The first two terms of the equation are known, but the exchange correlation function can only be approximated.

2.6.1 Functionals

As the exchange correlation functional is not known, an additional approximation must be used. This can be a cause of significant error in DFT calculations as the chosen functional has a great effect on the outcome of the calculation, and different functionals can give very different results, so choosing the appropriate functional is of utmost importance. Commonly used functionals include the Local Density Approximation (LDA) and the Generalised Gradient Approximation (GGA).

The LDA assumes that the exchange correlation functional per electron is equivalent to that of a homogeneous electron gas with a given electron density $\rho(r)$. This method is able to reproduce systems where the electron density does not resemble a homogeneous electron gas, in part due to the cancellation of errors when calculating the various energy contributions.

LDA generally overestimates binding energies and underestimates band gaps, therefore when these properties are of interest, such as when studying the band-gap in semiconductors, another approximation is used. This is commonly GGA (Equation 2.15). Unlike LDA, GGA takes into account variations in the local density $\rho(r)$, and belongs to a class of functional known as "gradient correlated" functionals, where GGA is the simplest. There are multiple forms of the GGA functional, some of the most popular being PBE and PBE-Sol, which are used in this work.

$$E_{xc}^{GGA}[\rho(r)g(r)] = \int \rho(r)\epsilon_{xc}^{GGA}(\rho(r), \nabla\rho(r))dr \tag{2.15}$$

There are higher levels of approximation not discussed here, but through these steps DFT can solve a great number of problems in computational chemistry. In solid state chemistry there is an additional issue which needs to be considered. When determining properties of solid state systems, the DFT calculation treats the lattice as an infinite cell. As the wavefunction extends infinitely over the lattice, an infinite number of basis sets would be required to accurately simulate the system. K-space and periodic boundary conditions are therefore implemented.

2.6.2 K-space and the Periodic Boundary

The use of periodic boundary conditions allows the crystal to be considered finite, and periodic boundary conditions also increase the speed of the calculation by utilising reciprocal space (k-space) rather than real space. In real space, the lattice vectors *a*, *b*, and *c* are used to describe the lattice of the crystal system, whereas the reciprocal cell is defined as the Brillouin zone in reciprocal space. Within the Brillouin zone a complete description of the wavefunction can be provided in accordance with Bloch's theorem, which states that the wavefunction of an electron (i) within a periodic field can be written as the product of two parts; a wave-like term (e^{ikr}) and a function with the same periodicity as the external field ($f_i(r)$), as described in Equation 2.16.

$$\psi_i(r) = e^{ikr} f_i(r) \tag{2.16}$$

Where k describes the wave vector in the Brillouin zone and r describes the position vector. As ψ is a function of k, a finite number of k values can be

sampled to describe the system, with less points in k-space describing a larger area in real space.

In order to achieve convergence in DFT and accurately simulate a crystal structure there are several criteria which need to be fulfilled:

- The selection of an appropriate type of functional
- The selection of an appropriate number of k-points
- The lowering of the internal force and pressure of the system

It is through the fulfilment of the first two criteria that the third can be successfully achieved.

Chapter 3

Results and Discussion: The Potential Model

"For a moment, nothing happened. Then, after a second or so, nothing continued to happen."

Douglas Adams
The Hitchhiker's Guide to the Galaxy

3.1 Development of Potential Models for Perovskite Halides

The primary objective of this project is to use computational techniques to develop an interatomic potential model for the $Cs(Pb,Sn)(I,Br,Cl)_3$ series, including all possible structures for analysis of phase behaviour and the effect of dopants. Although this has not been achieved before, several related systems have been modelled and this potential set can therefore be used as a starting point for the investigation. A potentials-based approach to analysing the phase behaviour of the $Cs(Pb,Sn)(I,Br,Cl)_3$ series has two main advantages over a DFT-based approach. Firstly, interatomic potential models have the ability to investigate much larger systems with a much smaller computational cost. Secondarily, the inclusion of temperature and the ability to run large timescale molecular dynamics simulations is a significant advantage of interatomic potentials over DFT. Developing an interatomic potential model means that once the initial objective of examining the phase behaviour of the

series has been completed, the model can be then utilised as a tool for additional complex problems. Chief amongst these is the investigation of defects and ion migration in the systems, as this has particular implications for photovoltaic viability. Additionally the model can then be applied to answering more unanswered questions, such as the behaviour of clusters and interfaces, which a purely DFT-based approach would struggle to fully examine.

Table 3.1: Interatomic Buckingham potential model for binary halides from Sangster *et al.*[76,77] The functional form of the Buckingham potential is: $\Phi(r) = Aexp(\frac{-r}{\rho}) - \frac{C}{r^6} + \frac{q_1 q_2}{4\pi\epsilon_0 r}$

Interaction	A (eV)	ρ (Å)	C (eV Å^6)
Rb^+ – Rb^+	70180000000.0	0.1119	91.84
Rb^+ – F^-	2114.0	0.3102	45.90
Rb^+ – Cl^-	4592.0	0.3265	125.44
Rb^+ – Br^-	4253.0	0.3460	197.34
Rb^+ – I^-	4534.0	0.3650	271.30
Cs^+ – Cs^+	0.3584e17	0.0843	240.34
Cs^+ – F^-	1327.0	0.3538	78.60
Cs^+ – Cl^-	4717.0	0.3455	204.62
Cs^+ – Br^-	4413.0	0.3644	321.24
Cs^+ – I^-	4913.0	0.3814	480.06
F^- – F^-	22940.0	0.2303	23.89
Cl^- – Cl^-	3361.0	0.3564	193.92
Br^- – Br^-	2745.0	0.3986	454.90
I^- – I^-	2532.0	0.4474	1015.26

Several potential models have been developed for alkali halides and related structures, which can possibly be adapted to fit the caesium halide perovskites. Sangster et al.[76,77] produced a shell model Buckingham potential, for the entire range of binary alkali halides, from which the Cs-X, Rb-X and I-I potentials are most useful for modelling these perovskites (Tables 3.1 and 3.2). As they have been developed for binary systems, the potentials would have to be adjusted for ternary systems. This would be a good starting point for a fitting process due to the similar compositions of the structures and the range of potentials available.

Table 3.2: Core/shell charges and spring constants for binary halides from Sangster *et al.*[76,77]

Atom	Core	Shell	Spring (kg/s^2)
Rb	5.9147	-4.9147	222.98
Cs	7.6337	-6.6337	244.84
F	0.6810	-1.6810	41.76
Cl	1.6532	-2.6532	31.33
Br	1.7370	-2.7370	23.80
I	2.0332	-3.0332	19.59

The alkali halides have also been examined by Catlow *et al.*,[78] though they do not consider any caesium compounds (Tables 3.3 and 3.4). As such, if these potentials were used as the basis of the perovskite halide potential set, then a separate Cs-X potential would have to be employed that may not fit as well with the other potentials as a simultaneously fit potential would. This issue will still have to be addressed with the Pb-I potential as neither of these or the Sangster potentials contain one of these.

Table 3.3: Interatomic Buckingham potential model for alkali halides from Catlow *et al.*[78]

Interaction	A (eV)	ρ (Å)	C (eV Å^6)
Rb^+ – Rb^+	6808.10	0.2704	C of anion
Rb^+ – F^-	2209.30	0.2945	0.00
F^- – F^-	1127.70	0.2753	69.83
Rb^+ – Cl^-	3559.90	0.3233	0.00
Cl^- – Cl^-	1227.20	0.3214	201.20
Rb^+ – Br^-	4169.90	0.3321	0.00
Br^- – Br^-	2948.20	0.3164	261.40
Rb^+ – I^-	5282.00	0.3431	0.00
I^- – I^-	5502.50	0.3066	400.60

Pb-X potentials have been developed by Islam[79] and Mattoni *et al.*[80] The Islam potential set (Tables 3.5 and 3.6) was developed for examining defects in PbFCl, and therefore is useful for chlorides and fluorides but does not cover iodide compounds, which is covered by the Mattoni potentials – developed

Table 3.4: Core/Shell charges for the alkali halides from Catlow *et al.*[78]

Atom	Core	Shell	Spring (kg/s^2)
Rb	126.3	-125.3	121460.0
F	0.339	-1.339	37.98
Cl	1.485	-2.485	29.38
Br	1.705	-2.705	24.66
I	3.087	-4.087	39.95

for modelling methylammonium lead iodide perovskite and as such is ideally suited for modelling halide perovskites (Table 3.7). One problem with the Mattoni potentials is the atoms being rigid-ion, and therefore polarisability within the atoms is not fully taken into account. Mattoni also utilised a Lennard-Jones potential in their model as additional constraints, so using purely the Buckingham potentials may not be indicative of all the interactions occurring in the structure.

Table 3.5: Interatomic Buckingham potential model for lead halides from Islam[79]

Interaction	A (eV)	ρ (Å)	C (eV Å^6)
Pb^{2+} – Pb^{2+}	81035.5	0.1003	79.1
Pb^{2+} – F^-	2973.1	0.2833	0.0
Pb^{2+} – Cl^-	2381.9	0.3373	0.0
F^- – F^-	2008.6	0.1937	67.5
F^- – Cl^-	556.83	0.3707	48.8
Cl^- – Cl^-	9909.3	0.3112	183.5

Table 3.6: Core/Shell charges for the lead halide potential model from Islam[79]

Atom	Core	Shell	Spring (kg/s^2)
Pb	6.559	-4.559	297.9
F	1.390	-2.390	204.6
Cl	1.515	-2.515	188.2

Table 3.7: Interatomic Buckingham potential model for methylammonium lead iodide from Mattoni *et al.*[80]

Interaction	A (eV)	ρ (Å)	C (eV Å^6)
Pb^{2+} – Pb^{2+}	70359906.629702	0.131258	0.0
Pb^{2+} – I^-	103496.133010	0.321737	0.0
I^- – Cl^-	22793.338582	0.482217	696.949542

3.2 Derivation of Interatomic Potentials

As none of the current literature potential sets are completely adequate for modelling the $Cs(Pb,Sn)(I,Br,Cl)_3$ series, a new potential model was developed. The developed model features single cation-cation and cation-anion Morse potentials that can be used to accurately model all the known phases of the $Cs(Pb,Sn)(I,Br,Cl)_3$ series.

All known phases in the $Cs(Pb,Sn)(I,Br,Cl)_3$ series were first optimised using DFT, with the potential model being trained to reproduce these DFT derived structures. During the process, the structures were also compared with experiment to check for accuracy. Where available, experimental bulk moduli, elastic and dielectric constants were also incorporated in the fitting procedure to in order to make sure all the physical properties of the materials were accurately modelled. Additionally, the relative energy differences between the structures were reproduced in the model.

In order to best reproduce the observed structures, a rigid-ion, partial charged model was used. Using partial charges meant there was much greater agreement with structural data than formal charges, due to the increased covalency in the system that needed to be taken into account. Despite the issues with using rigid ions, the model did not utilise shells as this significantly decreased the number of variables that had to be taken into account in the procedure, and also meant that the model could be used with a wider range of computational programs. The Mulliken charges[81] of $CsPbI_3$ were calculated using the DFT software VASP[82] and the partial charges of the potential model were based upon these. Caesium was determined to have a partial charge of +1, lead as +0.5 and iodine as -0.5. Bromine and chlorine were given the same charge as iodine, and tin the same charge as lead in order to facilitate

Table 3.8: Morse potential parameters for the developed $Cs(Pb,Sn)(I,Br,Cl)_3$ series potential model. The functional form of the Morse potential is: $V(r) = D_e[(1 - exp(-a(r - r_0)))^2 - 1]$

Interaction	D (eV)	a (Å-2)	r0 (Å)
Cs – Cl	0.157021	0.958243	4.223457
Sn – Cl	0.356816	1.174471	3.062151
Pb – Cl	0.431446	1.466672	3.004852
Cl – Cl	0.086980	1.004988	4.280670
Cs – Br	0.114032	1.016207	4.241085
Sn – Br	0.360954	1.389344	3.012245
Pb – Br	0.398803	1.478416	3.080280
Br – Br	0.084855	1.142631	4.502942
Cs – I	0.027407	1.204640	4.671066
Sn – I	0.347124	1.301832	3.230214
Pb – I	0.385330	1.339656	3.294995
I – I	0.099521	1.447466	4.515778

the modelling of substitutional defects and intermediate phases.

To create the interatomic potential models, a particle swarm optimisation algorithm was written in Python using a series of structures he calculated using DFT as a starting point and the molecular dynamics code LAMMPS to optimise the structures. Using a starting population of 500 particles, with each particle having a random starting configuration of interatomic potentials, all the possible structures in the perovskite halide series were modelled. The criteria for optimisation included a good fit to lattice parameters, sensible relative lattice energies, small internal pressures and minimal forces. A sum of squares was calculated for each particle and the best fitting particle in the population was determined. Over successive population iterations the interatomic potentials were updated and the energy landscape was explored. As the landscape was explored a global best fit, where no lower sum of squares could be found, was identified. This process created a potential model (Table 3.8) with a low sum of squares that was able to accurately reproduce all the modelled phases as well as their physical properties.

The model, being both rigid-ion and partial charge, cannot be used to calculate accurate defect energies, but is very accurate for structural analysis. As such, the model has been used to generate accurate structural models as a starting point for assessing the phase stability of each of the phases. Further refinement of the model would be needed to get accurate defect energies as with a partial charge model the charge on any vacancy or interstitial defect would be incorrect. The model can be effectively used for examining substitutional defects, and with interest increasing in variable 'A' site triple and quadruple cation perovskites, this model would be an ideal analytical tool.[29,55]

3.2.1 Structural Modelling of Cs(Pb,Sn)(I,Br,Cl)$_3$ Phases

$CsPbI_3$ has three phases of interest that were included in the potential model. DFT structures of two perovskite phases; cubic and orthorhombic, as well as the non-perovskite delta phase were incorporated in the model, with bulk modulus and lattice energy being additional parameters in the fitting run. These structures are described previously, with the perovskite phases having corner-sharing PbI_6 octahedra and the delta phase being edge-sharing. For each phase, the model managed to replicate the DFT lattice parameters to very high degrees of accuracy, with almost all having less than 1 % difference between DFT and potentials. For the phases that exist experimentally, cubic perovskite and delta phase, the model was also compared to the experimental structures will less than 1 % difference between the experimental and calculated structures. Table 3.9 summarises the calculated lattice parameters and their relationship with experiment.

The lattice energies of the phases from the fitting run were trained across the entire structure series to DFT energies, and the energy differences between each structure was also a constraint in the optimisation run. Each phase of $CsPbI_3$ was fit to a relative energy scale, which includes all the other structures in the investigation. This means that doping between all the materials can be more accurately modelled and intermediate phases can also be examined. Figure 3.1 shows the energy scale with each structure in the series and the agreement between the potential model and DFT. The relative energy scale used cubic (α) $CsSnCl_3$ as the zero point which all the others were fit to.

Table 3.9: Comparison between experimental (Stoumpos *et al.*[14]), DFT and interatomic potential lattice energies for $CsPbI_3$ showing the accuracy of the potential model.

Phase	Param	Exp (Å)	DFT (Å)	Potentials (Å)	% Diff (DFT)	% Diff (Exp)
Cubic	a	6.290	6.272	6.264	0.13	0.41
	b	6.290	6.272	6.264	0.13	0.41
	c	6.290	6.272	6.264	0.13	0.41
Delta	a	4.801	4.770	4.818	1.01	0.35
	b	10.458	10.460	10.375	0.82	0.80
	c	17.776	17.745	17.759	0.08	0.09
Ortho	a		8.954	8.938	0.18	N/A
	b		12.417	12.373	0.35	N/A
	c		8.414	8.350	0.77	N/A

It can be seen here that for the iodides and bromides there is a very high degree of accuracy, and the chlorides are slightly less accurate. This is due to the significant changes in the level of covalency between the iodides and chlorides making the partial charges used, which were based on $CsPbI_3$, become less accurate as the halide ion changed. At present there is still little experimental information about the lattice energies and bulk moduli of these materials, though theoretical study of the structures has been undertaken. Verma and Kumar[83] have studied the theoretical bulk moduli of cubic perovskites including the ones in this series (Table 3.10); though these calculations involve numerous approximations which may not be truly physical. The result of their calculations back up experimental knowledge about bulk moduli and their relationship to the lattice constant of the material, and agree with other theoretical calculations of the studied properties.

What is apparent from these results is both the relationship between bulk modulus (BM) and lattice constant, one decreases at the other increases, and the small BM values calculated for all of the $CsPbX_3$ materials. Compared to common cubic perovskite oxides, such as $SrTiO_3$ (BM = 179) and $BaTiO_3$ (BM = 162), the BM is particularly small, which suggests the halide ion has a considerable effect on the mechanical properties of the structure. Other

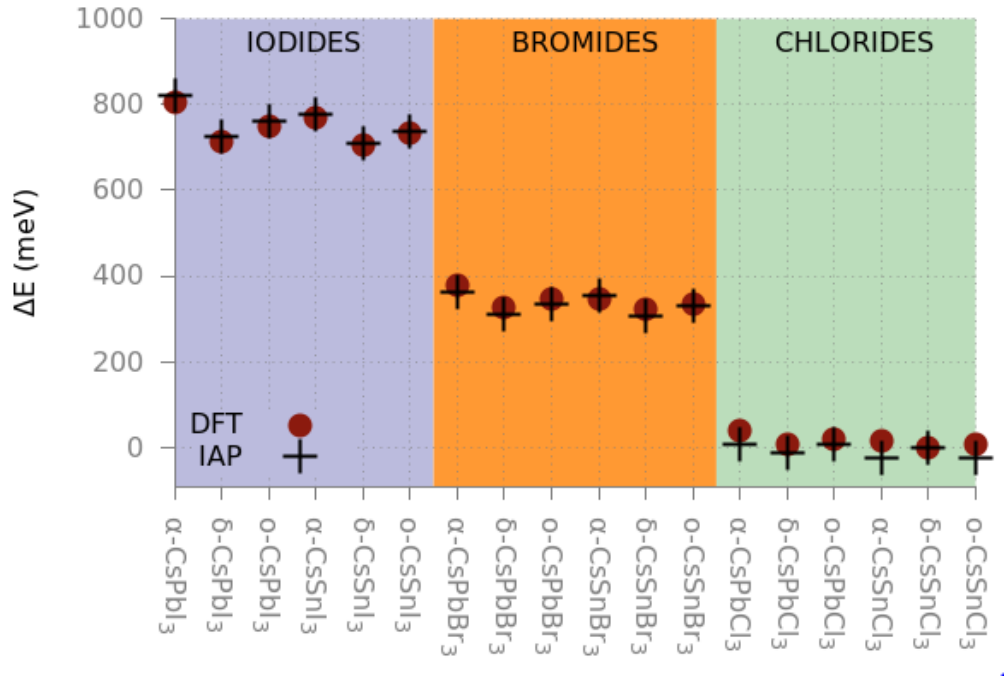

Figure 3.1: Structures of the Cs(Pb,Sn)(I,Br,Cl)$_3$ series, showing the relative lattice energies using cubic $CsSnCl_3$ as the zero point. The DFT energies (dots) are compared with the measured energies from the interatomic potentials (crosses) showing the accuracy of the fitted model.

caesium halide perovskites studied, such as $CsCaF_3$ (BM = 49) also have small bulk moduli, which supports this conclusion, but the lead halides have the smallest overall. This suggests that the lead ion also has a significant effect.[83] The calculated bulk moduli from the model, shown in Table 3.11, has good agreement to the literature bulk moduli in Table 3.10 for $CsPbI_3$, the literature value being 19.8 GPa compared with a calculated range of 15.88 – 22.15 GPa for the three phases. Additionally, the calculated lattice energies show the delta phase as the lowest energy and cubic phase as the highest, agreeing with experimental observations.

The accurate modelling of $CsSnI_3$ was also of high priority due to the potential for tin to replace lead in solar materials and lower the toxicity. Like $CsPbI_3$, the cubic perovskite, orthorhombic perovskite and orthorhombic delta phase were included in the model, with the lattice parameters showing very good agreement with DFT, within 1 %. Again the experimental lattice parameters were also compared to in order to confirm the accuracy of the model,

Table 3.10: Theoretical bulk moduli (BM) of cubic $CsPbX_3$ (X = I, Br, Cl, F) from Verma and Kumar[83].

Structure	BM / GPa
$CsPbI_3$	19.8
$CsPbBr_3$	23.5
$CsPbCl_3$	25.8
$CsPbF_3$	36.0

Table 3.11: Calculated lattice energies (LE) and bulk moduli (BM) of the $CsPbI_3$ phases using the interatomic potential model.

Polymorph	LE (eV)	BM (GPa)
c-$CsPbI_3$	-41.126	20.84
o-$CsPbI_3$	-41.701	15.88
δ-$CsPbI_3$	-42.085	22.13

with all three phases being within 2.5 % of experiment. This comparison is shown in Table 3.12.

The calculated lattice energies of the tin iodides in Table 3.13 have the same trend as experiment, and the bulk moduli agree with literature bulk modulus calculations for the perovskite halides.

3.2.2 Structural Modelling of Bromides and Chlorides

The bromides and chlorides were also incorporated within the model in order to investigate X site anion variation. Recent experimental work has shown the potential of mixed I/Br perovskites as photovoltaics, so modelling how the addition of Br and Cl affects the lattice is of particular interest.[13] Despite similarly good fit to experimental data as with the iodides, and accurate lattice energies as shown in Figure 3.1, the model is slightly less accurate for the bromides and chlorides.

The significantly decreased covalency of the other halide systems compared to the iodides means the partial charge model does not completely hold up. Ideally the partial charge of bromine and chlorine would be more negative than for iodine, but in order to preserve charge balance this level of accuracy had to be sacrificed in order to be able to model the entire set. A variable charge

Table 3.12: Comparison between experimental (M. Saliba *et al.*[29] and Trots *et al.*[31]), DFT and interatomic potential lattice energies for $CsSnI_3$ showing the accuracy of the potential model.

Phase	Param	Exp (Å)	DFT (Å)	Potentials (Å)	% Diff (DFT)	% Diff (Exp)
Cubic	a	6.206	6.165	6.189	0.39	0.27
	b	6.206	6.165	6.189	0.39	0.27
	c	6.206	6.165	6.189	0.39	0.27
Delta	a	4.763	4.693	4.731	0.82	0.67
	b	10.350	10.408	10.487	0.75	1.31
	c	17.684	17.617	17.578	0.22	0.60
Ortho	a	8.688	8.809	8.728	0.92	0.46
	b	12.378	12.300	12.340	0.33	0.31
	c	8.643	8.391	8.443	0.62	2.34

Table 3.13: Calculated lattice energies and bulk moduli of the $CsSnI_3$ phases using the interatomic potential model.

Polymorph	LE (eV)	BM (GPa)
c-$CsSnI_3$	-40.660	21.207
o-$CsSnI_3$	-41.019	17.691
δ-$CsSnI_3$	-41.250	22.021

potential model such as ReaxFF would be able to model this more accurately and would eliminate the need for partial charges, but would be considerably more complex.[84] Additionally a reactive forcefield such as ReaxFF would not be able to be used with many simulation packages.

3.3 'A' Cation Size Variation in $CsPbI_3$

One of the key issues that the halide perovskites face is the instability of the perovskite phase of $CsPbI_3$ at room temperature. There is much debate about how to lower the phase transition temperature of $CsPbI_3$ in order to stabilise the perovskite phase, and it has been seen that changing the size of the 'A' site cation in perovskites can have major effects on the structure related to the Goldschmidt tolerance factor. $CH_3NH_3PbI_3$ (MAPI) has a larger 'A' site cation, and has a tetragonal perovskite structure at room temperature. $CH(NH_2)_2PbI_3$ (FAPI) is also perovskite at room temperature, with a significantly larger 'A' site cation than caesium.

The developed potential model is ideal for simulating the bulk properties of $CsPbI_3$, and optimisation techniques as discussed in the methodology can be used to determine the lattice energy of the relaxed bulk crystal. In Figure 3.1 it is shown that the relative lattice energies of the different species in the $Cs(Pb,Sn)(I,Br,Cl)_3$ series can be used to fit an energy scale to ensure the physical properties of a system are being correctly modelled. In effect making sure that lower temperature phases of a material are more stable than higher temperature phases, which require more energy input to reach. This can be taken a step further when applied to comparing two separate phases at a single temperature, essentially the phase with a lower lattice energy at a given temperature is more stable and is more likely to form.

With this in mind, two $CsPbI_3$ structures were simulated using the model, one in the perovskite phase and one in the δ-phase, and their relative lattice energies examined. The calculations were undertaken examining the static bulk structures at 0 K. When initially simulating the two phases, the perovskite phase had the highest lattice energy, as was expected due to this phase being the high temperature phase. In order to then determine the effect of 'A'

site cation size on this relationship, a potential for a dummy atom termed 'fakeinium' was developed, with this atom placed on the 'A' site position in place of caesium. This potential initially had the same parameters as the Cs – I potential parameter as described in Table 3.8, but the 'r_0' equilibrium bond length parameter was varied by a set amount, increasing and decreasing the Cs – I bond length and simulating a change in size of the dummy atom. The variation in cation size could then be used to simulate the effect of increased sized cations such as MA^+ on the phase stability of the two phases. Figure 3.2 shows how the lattice energies of the two phases of $CsPbI_3$ change on varying the interatomic separation of the dummy atom. The interatomic separations corresponding to several 'A' site cations have been noted, showing where the ionic radius of the dummy atom corresponds with that of the alkali metals, MA^+ and FA^+. The respective ionic radii of the alkali metals of interest are notes in Figure 3.3. At the "Cs^+" line, the interatomic separation and therefore the potential of the dummy atom is identical to that of the Cs – I potential.

The results presented in Figures 3.2 and 3.4 indicate two main points. Firstly, the interatomic separations relating to $CsPbI_3$ and $RbPbI_3$ both lie within the region of relative delta phase stability, which agrees with experiment. To stabilise the perovskite phase in $CsPbI_3$ it is clear that the average interatomic separation between the 'A' site cation and the PbI_6 cage needs to be either increased or decreased. $KPbI_3$ has a small enough interatomic separation to have a more stable perovskite phase, and has previously been identified as a possible photovoltaic, though no photovoltaic device was synthesised.[85,86] Doping $CsPbI_3$ with smaller cations such as potassium may have this stabilising effect, but as the efficacy of $KPbI_3$ as a photovoltaic and even the stability of a potassium perovskite is highly unlikely, as this would decrease the Goldschmidt tolerance factor.

The second key conclusion of this is that at interatomic separations above approximately 4.8 Å, the perovskite phase is more stable and has a lower energy than the delta phase. The model predicts that MA^+ and FA^+ cations will both form perovskite structures as they have interatomic separations above this value, which agrees with experiment where $MAPbI_3$ is shown to be a

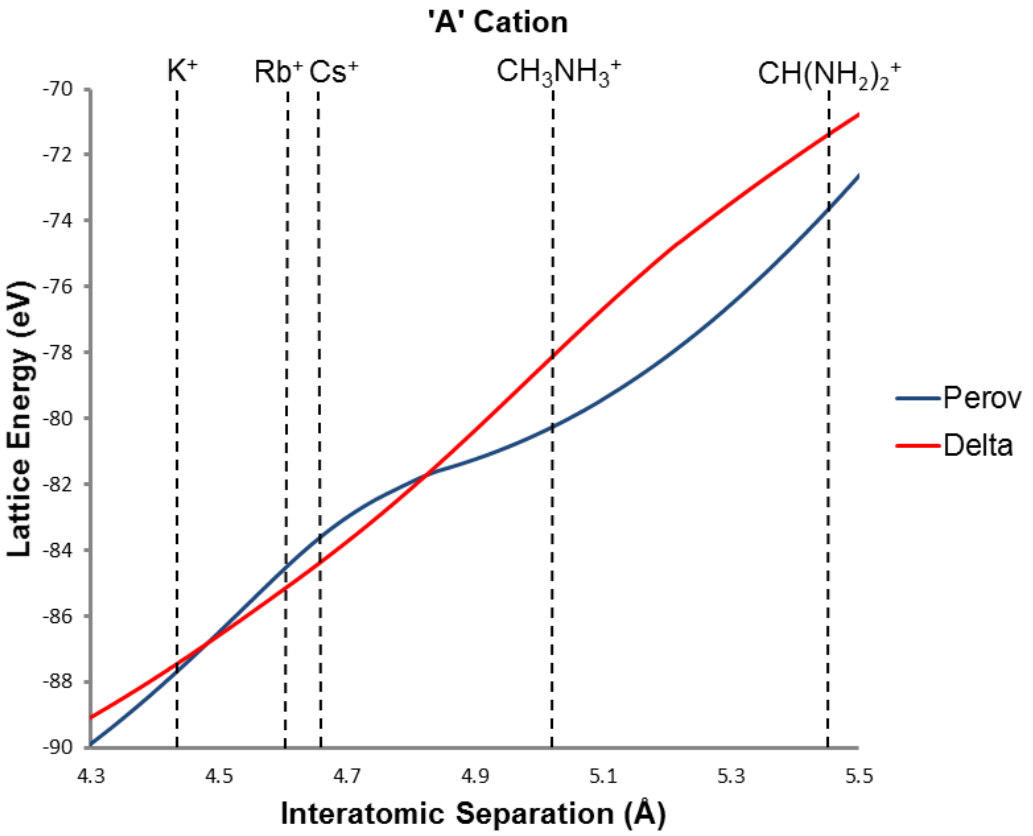

Figure 3.2: Lattice energies of both perovskite (blue) and delta (red) phases of $CsPbI_3$ as a function of interatomic separation. The interatomic separations corresponding to common 'A' site cations are noted for reference.

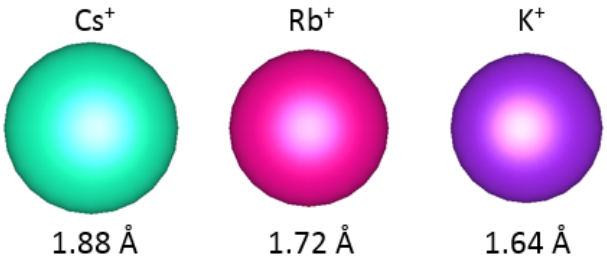

Figure 3.3: Relative ionic radii of Cs^+, Rb^+ and K^+

tetragonal perovskite and $FAPbI_3$ a cubic perovskite at room temperature, with no delta phase present.[14,30] Using this information, it can be seen that doping of $CsPbI_3$ with MA^+ will stabilise the perovskite phase. The model postulates that even larger organic cations such as FA^+ would be even more effective in stabilising the perovskite phase, and smaller concentrations of dopant would be needed to achieve the desired effect. A mixed-phase MAPI-FAPI hybrid perovskite would be the most ideal for phase stabilisation, and

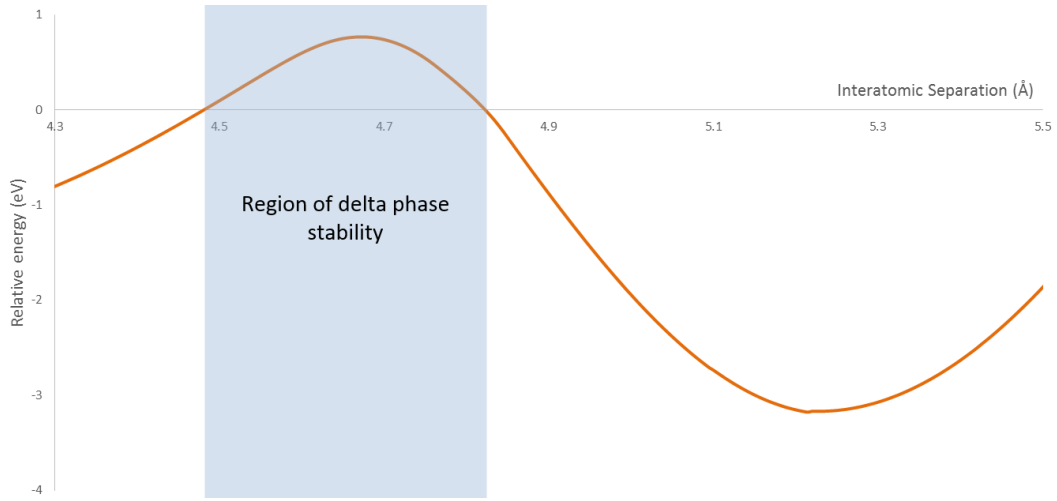

Figure 3.4: Relative energies of the delta and perovskite phases of $CsPbI_3$ as a function of interatomic separation, the region where the delta phase is stabilised is shown in blue. At the zero point the lattice energies of the two phases are identical, with the delta phase being lower in energy when the relative energy is positive, and the perovskite phase lower in energy when the relative energy is negative.

this is evidenced by the several of the current highest efficiency solar cells being mixed phase hybrid perovskites.[26,27,29]

The average interatomic separation of these structures would be in the region where the perovskite phase is most stable against the delta phase, and the efficiencies of solar cells with a mixed-cation perovskite semiconductor being amongst the highest of all perovskite solar cells is evidence of this, as seen in Table 3.14.

Table 3.14: Various halide perovskite compositions in order of certified photovoltaic device efficiency.

Structure	Efficiency (%)	Year	Reference
$Cs_{0.2}FA_{0.8}PbI_3$	15.69	2016	C. Yi *et al.*[23]
$Cs_{0.2}FA_{0.8}PbI_{2.84}Br_{0.16}$	17.35	2016	C. Yi *et al.*[23]
$(FAPbI_3)_{0.85}(MAPbBr_3)_{0.15}$	17.9	2016	J. Seo *et al.*[26]
$(FAPbI_3)_{0.85}(MAPbBr_3)_{0.15}$	18.4	2015	N. J. Jeon *et al.*[27]
Cs, Rb, MA, FA Quadruple Cation	20.5	2016	M. Saliba *et al.*[29]
$Cs_{0.1}(MA_{0.17}FA_{0.83})_{0.9}Pb(I_{0.83}Br_{0.17})_3$	21.1	2016	M. Saliba *et al.*[55]

This model, though only a starting point, could be built upon to determine which compositions of mixed-cation perovskite would be stabilised in the perovskite phase, informing experimentalists when determining possible new compositions, and is a significant first step in establishing a phase diagram for the perovskite halide series. The effect of temperature could be analysed more, and a second step for this methodology would be to examine the variation of temperature for a number of different sized cations to fully understand how a phase diagram for this series would form. An investigation into temperature effects using this model would be a fundamental leap forward and would open the way for the production of a full phase diagram, one of the key aims of this project.

3.4 Conclusions

Through this investigation an interatomic potential model for the $CsPbI_3$ series has been successfully developed, which has not been achieved before. A rigid-ion Morse potential model was used, and the degree of covalency in $CsPbI_3$ was found to have a major effect on the structure, leading to the final model using partial charges. The tin, bromide and chloride analogues of $CsPbI_3$ were also incorporated into the model to a high degree of accuracy, as well as the tin analogues of the entire series. Additionally within the model both the structures of the perovskite and non-perovskite phases of each system were accurately reproduced, as well as the relative energies of each individual phase.

The variation of 'A' site cations has been studied, with the effect of changing cation size on the lattice energy being examined and forming the basis for a full investigation into the phase behaviour of the entire $Cs(Pb,Sn)(I,Br,Cl)_3$ series. The key conclusions of this work are that cations larger than the size of Cs^+ stabilise the perovskite phase in $CsPbI_3$, and that MA^+ and FA^+ have ideal cation sizes for this purpose. It was also found that mixed cation perovskites have the ideal average interatomic separation for perovskite phase formation. This is confirmed experimentally by the prominence of the perovskite phase in these systems at room temperature.

The next step in investigating this 'A' site variation is to model the effect on the PbI_6 cage surrounding the 'A' sites and to further probe why there

is increased efficiency and stability in these systems. This will be discussed further in chapter 4.

3.4.1 Further Work

The results of this project open up avenues for subsequent work with $CsPbI_3$. The potential model can be used to investigate the formation of defects within the structure and how this affects the photovoltaic properties. The model can be used to show trends within the series and further see how the size variation affects the band gap and ion migration properties.

Similarities to other perovskite phases such as double perovskites with potential as photovoltaics can also be investigated, with the double perovskite Cs_2AgBiX_6 (where X = Br, Cl) showing promise as a lead free perovskite semiconductor.[87,88] Layered Ruddlesden-Popper perovskites such as $(BA)_2(MA)_{n-1}Pb_nI_{3n-1}$ (where BA = butylammonium cation) are also of increasing interest in the solar community.[89] This work can be built upon to create a comprehensive overview of how this structure variation affects the defect properties of the materials and their potential as photovoltaics. Other unanswered questions, such as the effect of cation mixing on local structure and the surface adsorption properties of MAPI and $CsPbI_3$ can also be studied building on the results of this work.

Additionally, the developed potential model can be used to create a full phase diagram of these systems, which would be of great use when determining the most ideal composition for photovoltaic applications. Knowledge of the full phase diagram would mean knowledge of which compositions have a stable perovskite phase at room temperature, and would inform further investigations as the search to find the most stable composition for use in solar cells continues.

Chapter 4

Results and Discussion: Octahedral Locking

"Perhaps I'm old and tired, but I always think that the chances of finding out what really is going on are so absurdly remote that the only thing to do is to say hang the sense of it and just keep yourself occupied"

Slartibartfast

The Hitchhiker's Guide to the Galaxy

4.1 Octahedral Tilting

The primary aim of this section of the project is to investigate the effect of 'A' site cation doping on the tilt structure of doped $CH(NH_2)_2PbI_3$ (FAPI). The level of octahedral tilting in the halide perovskites has an effect on now wide the band gap of the semiconductor is, so tuning this tilting is a key area of interest when improving the efficiencies of solar cells.[90]

The work in this section is a collaboration between the research groups of professor Saiful Islam and professor Alison Walker, with the aim of producing a research article. The molecular dynamics and DFT calculations were run by myself, Dr Chris Eames and Dr Dibya Ghosh. The Python coding and tilting analysis was undertaken by myself, with Dibya Ghosh assisting with running the analysis scripts and collecting the vibrational and RDF data.

These mixed cation systems have generally improved performance over their parent compounds, and this section aims to investigate this further. The origin of this performance enhancement has three possible mechanisms:

1. Lowering of the Gibbs free energy due to the entropy of mixing.[23,59]
2. Lowering the Goldshmidt tolerance factor due to the tilting of the octahedra on doping with smaller cations.[60,61]
3. Reducing the strain in the crystal through strain-relieving relaxation.[62]

However, lattice and A-site cation dynamics and their coupling have so far not been considered in detail, even though halide perovskites are found to be highly dynamical systems.[91] In FAPI the inorganic PbI_6 octahedral framework undergoes octahedral (Glazer) tilting with a time period of ≈0.2-1.5 ps.[92] The FA^+ molecular ions on the 'A' site in the structure undergo rotational or tumbling motion inside the cage (time period 2-3 ps), and their internal bonds undergo dihedral rotation and vibration at a high frequency (time period 10-20 fs).[92] The impact of this considerable amount of motion upon the structure and properties of mixed A-cation perovskites, however, is not fully understood.

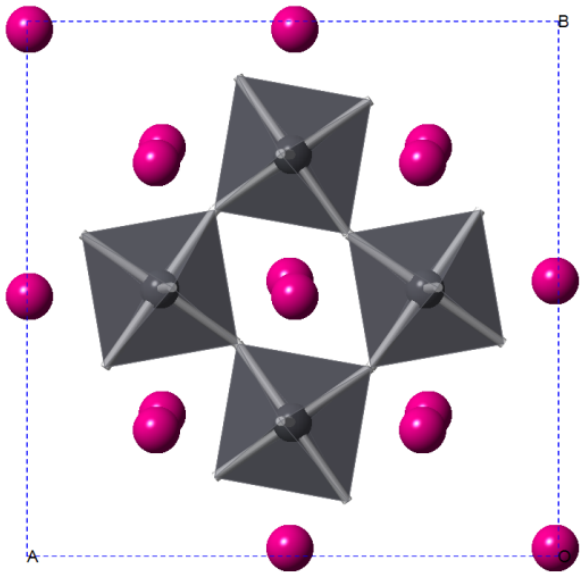

Figure 4.1: The orthorhombic $CsPbBr_3$ structure at 298 K viewed down the (001) plane. Adapted from Rodová *et al.*[34]

Within the ideal perovskite structure, each BX_6 octahedron is aligned completely with each other in the unit cell (Figure 1.6). With changes, such

as displacement or size variation, in 'A' and 'B' cations, these octahedra can become tilted with the cage becoming compressed. This brings the unit cell into lower symmetry states. For example the $CaTiO_3$ perovskite structure has tilted octahedra and subsequently a non-cubic unit cell with a *Pnma* space group, as does $CsPbBr_3$ (Figure 4.1).

Within the context of FAPI and perovskite solar cells, there are a number of questions which arise in relation to this tilting:

1. How does doping on the 'A' site change the tilt structure of FAPI?
2. How does this tilting affect the physical properties of the material?
3. How does this tilting affect the rotational motion of the $CH(NH_2)_2^+$ cation?
4. How does this tilting affect the degree of interaction between the central cation and the surrounding PbI_6 cage?

This investigation seeks to shed some light on these questions by using advanced *ab initio* molecular dynamics techniques to model the varying dynamics of the structure on doping with smaller cations.

4.2 Tilting in FAPI

The initial step in this investigation is to examine the effect on the perovskite structure of cation substitution on the 'A' site of FAPI. The criteria we use to examine the induced change in FAPI are the volume per formula unit and mean Pb-I-Pb bond angle over time. These criteria are chosen as the volume change will show the level of cell contraction, and the mean angle over time gives an indication of how tilted the octahedra are and subsequently how the band gap of the material will vary over time.[90] The cations chosen to substitute onto the 'A' site are MA^+ ($CH_3NH_3^+$), Cs^+ and Rb^+. From Figure 4.2 and Table 4.1 it can be seen that, when FA^+ is replaced by smaller cations, the cell volume is reduced.

For example, doping of 10 % Rb^+ (the smallest in size among the cations considered) causes a volume reduction of 2.2 %. The effect is less pronounced

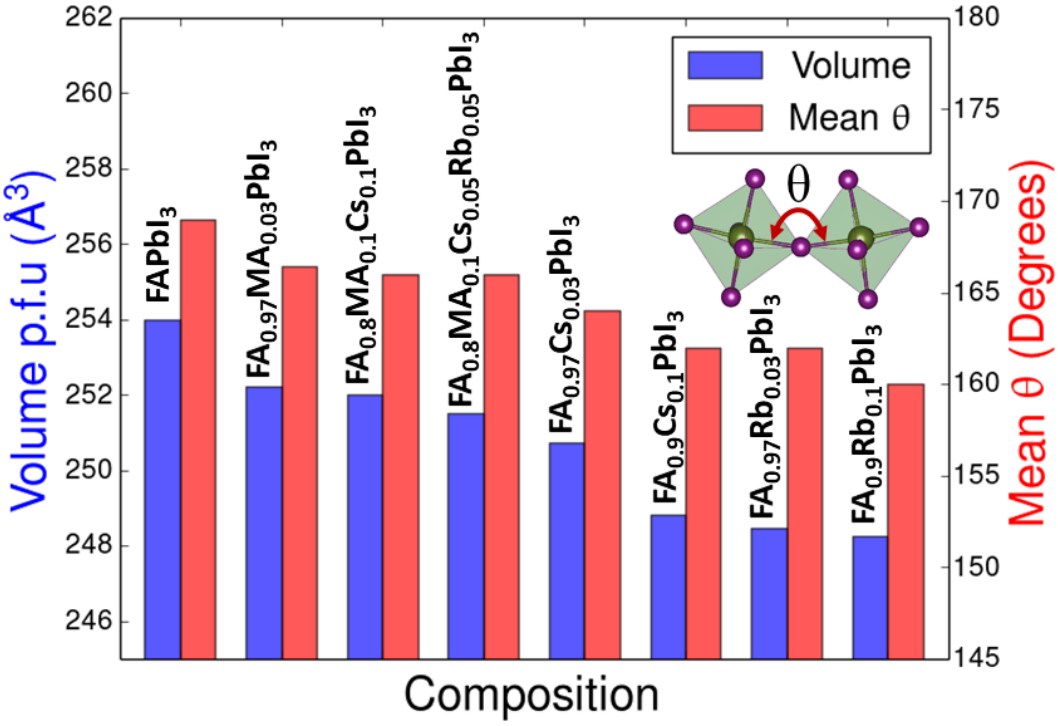

Figure 4.2: Dynamically averaged properties at 300K of lead iodide perovskites with various 'A' site compositions of FAPI doped with MA^+, Cs^+ and Rb^+. Equilibrium volume per formula unit (blue bars) and mean Pb-I-Pb angles over time (red bars). Inset shows the octahedral tilting, defined as (180-θ)°.

when the intermediate sized cation MA^+ is involved. Doping of 10% MA^+ and 10 % Cs^+ leads to a lower volume reduction of 0.8 %. The average cell parameters after equilibration are shown in Table 4.1. The deviation from the experimental values is less than 1 %. The origin of this volume contraction is associated with the tilting of the PbI_6 corner sharing octahedra. In the inset of Figure 4.2, the tilt angle between two corner sharing octahedra as been defined, which for an ideal cubic perovskite is 0°. Whilst the average crystal structure of FAPI is cubic,[30] locally the octahedra tilt away from the ideal geometry and form more orthorhombic regions.[91] These regions balance out to generate the cubic structure seen in experiment. In this simulation, FAPI adopts a tilted structure with an average tilt angle of 11°. It is found that as smaller cations such as Cs^+ and/or Rb^+ are introduced onto the 'A' sites, they are less able to fill space in the cage, and as a result the octahedra tilt further to pack space more effectively. For example, the average tilt angle increases from 11° in FAPI to 20° in $FA_{0.9}Rb_{0.1}PbI_3$.

Table 4.1: Equilibrated cell parameters and cell volume for parent and mixed 'A' site cation perovskites. Experimental lattice parameters are given in brackets.[30]

Composition	a=b (Å)	c (Å)	Volume p.f.u (Å)	Volume vs. $FAPbI_3$ (Å)
$FAPbI_3$	6.34 (6.36)	6.35 (6.36)	255.24	
$FA_{0.97}Cs_{0.03}PbI_3$	6.27	6.37	250.72	-1.3%
$FA_{0.9}Cs_{0.1}PbI_3$	6.25	6.36	248.83	-2.0%
$FA_{0.97}Rb_{0.03}PbI_3$	6.25	6.36	248.47	-2.1%
$FA_{0.9}Rb_{0.1}PbI_3$	6.25	6.35	248.26	-2.2%
$FA_{0.97}MA_{0.03}PbI_3$	6.30	6.35	252.23	-0.7%
$FA_{0.8}MA_{0.1}Cs_{0.1}PbI_3$	6.30	6.34	252.00	-0.8%
$FA_{0.8}MA_{0.1}Cs_{0.05}Rb_{0.05}PbI_3$	6.30	6.32	251.50	-1.0%

Figure 4.2 shows the shift in average Pb-I-Pb bond angle on dopant incorporation for every angle in our MD simulations, clearly demonstrating the trend on doping. For each MD frame, all the Pb-I-Pb bond angles were measured and binned in a histogram. Each histogram was normalised over the number of angles in the frame, then added to the overall histogram for the MD trajectory. As a final step, this histogram was normalised against the timeframe of the simulation.

With regard to lattice dynamics, the octahedra are found to undergo a rocking motion whereby the tilt angle of the corner sharing octahedra oscillates about the equilibrium position.[30] This accounts for the histogram not being centred over 180° in pure FAPI and there being an inherent tilt angle of $\approx 20°$ in the systems.

This rocking motion has also been studied, and a clear change in rocking motion on dopant incorporation can be seen, as shown in Figure 4.4, where the pure system oscillates more strongly over a larger range than in the Cs-doped system. There is a significant reduction in the amplitude of oscillation for mixed-cation $FA_{0.9}Cs_{0.1}PbI_3$

The emergent picture is that when the parent $FAPbI_3$ is doped by smaller cations, the octahedra tilt at a greater angle. Furthermore, this tilting is 'locked' in place and undergoes much more restricted rocking dynamics, with

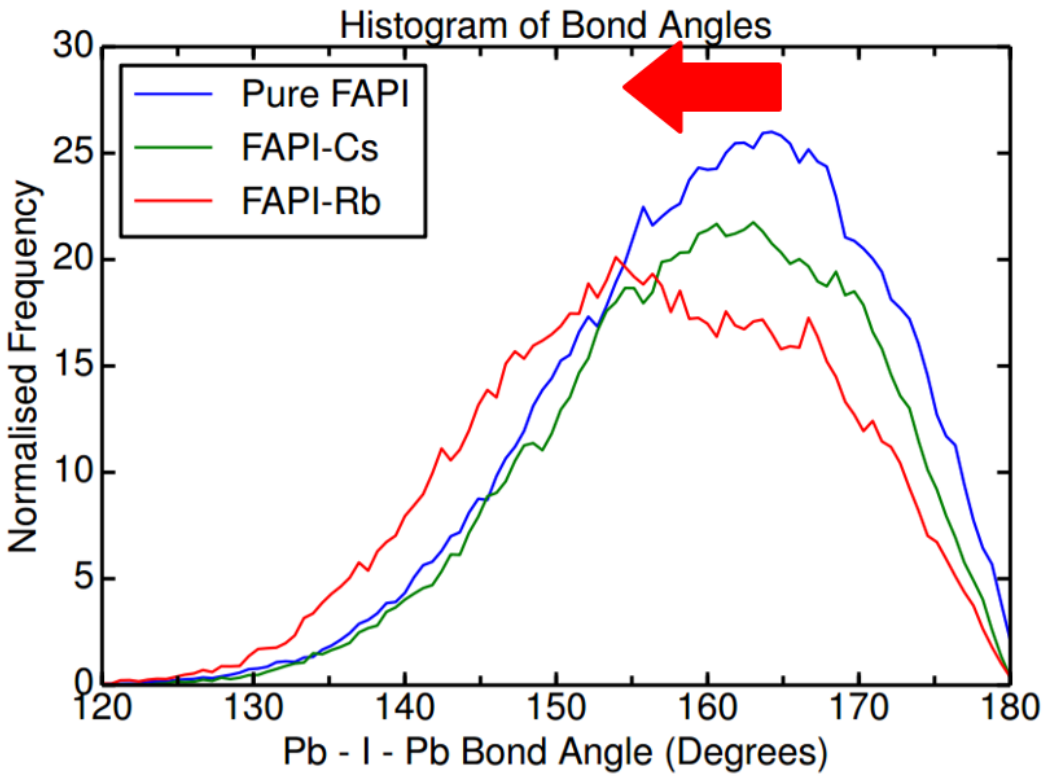

Figure 4.3: A histogram of the average tilt angles in MD simulations of pure FAPI (blue) and Rb/Cs doped FAPI where there is 10% doping level (red/green).

a noticeable change in the oscillation time.

Following the Glazer notation[18], time averaged geometries of these mixed cation systems exhibit locked 'in-phase tilting' (same-tilt) that is $a^0a^0c^+$ in the xy-crystal plane, as shown in figure 4.5. Related octahedral tilting or distortions are found in similar halide perovskites.[93,94]

This 'locking' structural feature can be further probed using the radial distribution function (RDF). The Pb-I nearest-neighbour peak in FAPI is at 3.18 Å, and remains unchanged on doping as shown in the RDF in Figures 4.6 and 4.7. This indicates that the internal bonding in the PbI_6 octahedra is unaffected by the doping as there is not a distance shift on doping. Therefore the the origin of the volume contraction does not lie in a contraction of the Pb-I bonds but in the increased tilting.

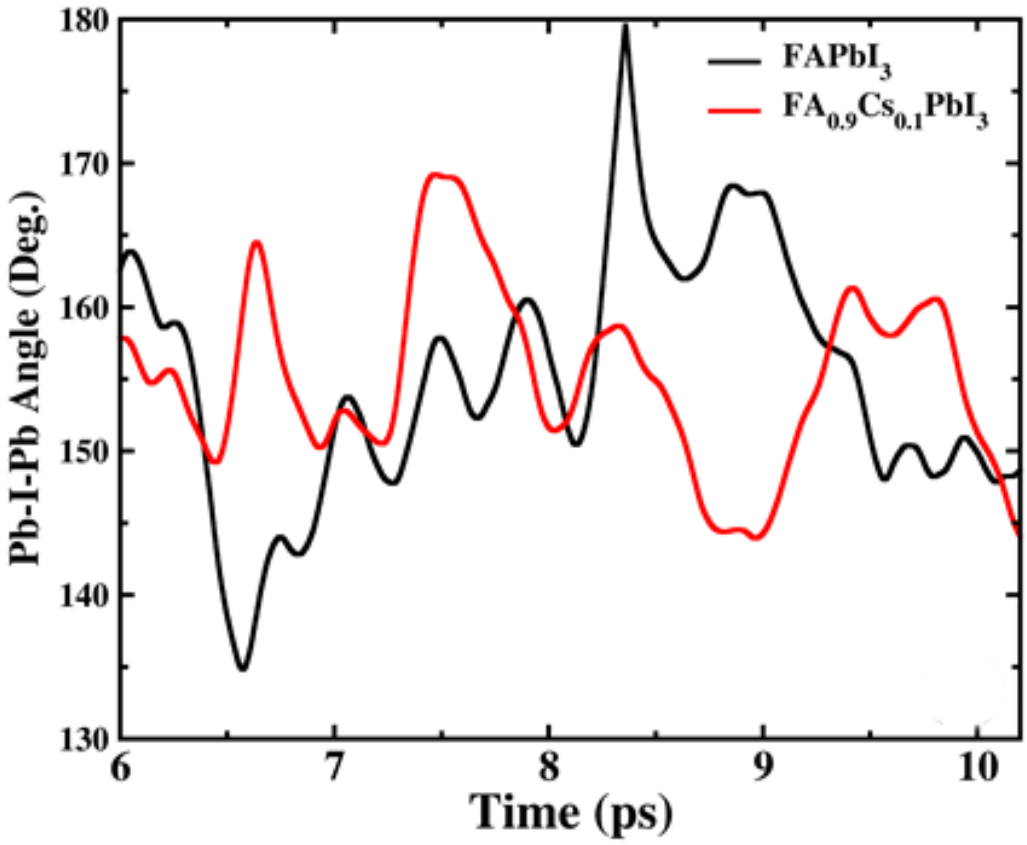

Figure 4.4: The variation in individual tilt angle with time in $FAPbI_3$ (black) and $FA_{0.9}Cs_{0.1}PbI_3$ (blue).

4.2.1 The Effect of Tilting on Bonding and Molecular Motion

In the mixed-cation systems, the increased cage tilting brings the hydrogen atoms of FA^+ cations into closer contact with the iodide ions, and one might expect greater N-H–I interactions and hence the degree of hydrogen bonding to increase. In order to examine this we calculated the vibrational spectrum of FAPI and Rb-doped FAPI, focussing on the region of the N-H stretching frequencies of FA^+ which appear at 3250-3550 cm^{-1}. An increase in hydrogen bonding in the system should induce a variation in the intensity of this stretching frequency.

Figure 4.8 shows the result of this calculation. The peak is split into two since the $NH_{(2)}$ group is a primary aliphatic amine and has symmetric and asymmetric (higher frequency) modes. The features of the computed vibrational spectra of FA^+ in the parent FAPI, including the peak splitting of

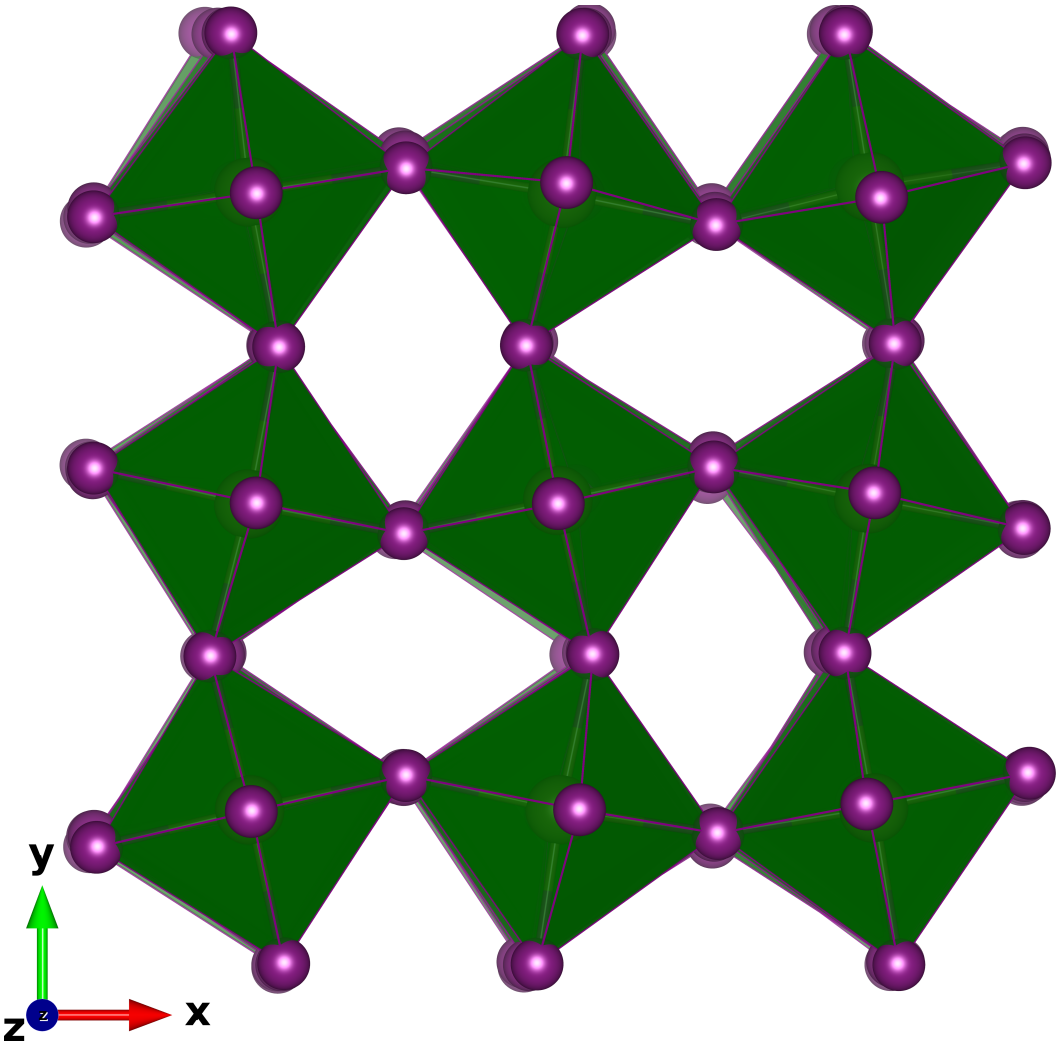

Figure 4.5: Time averaged structure of the inorganic framework of octahedral PbI_6 units in $FA_{0.9}Cs_{0.1}PbI_3$. Octahedra rotate mainly in the xy-plane so the the Pb-I-Pb bond angles along the [001]-axis of the crystal remain at 180°. The tilt pattern can be identified as 'in phase tilting' ($a^0a^0c^+$) according to Glazer notation. Key: Purple - Iodine; Green - PbI_6 octahedra).

$\approx$ 130 cm^{-1}, correlate well with recent experimental data of Zhou *et al.*[95] On doping with Rb^+ the intensity of the peak increases, and there is a slight red shift. This agrees with previous work by Matsui *et al.*[57] and is an indicator of increased hydrogen bond strength.[57,96] This is also evidenced in a broadening of the corresponding RDF for $FA_{0.9}A_{0.1}PbI_3$ where A = Cs^+ or Rb^+ as shown in Figure 4.9, as hydrogen bond formation affects the N-H bond length in the FA^+ cation.

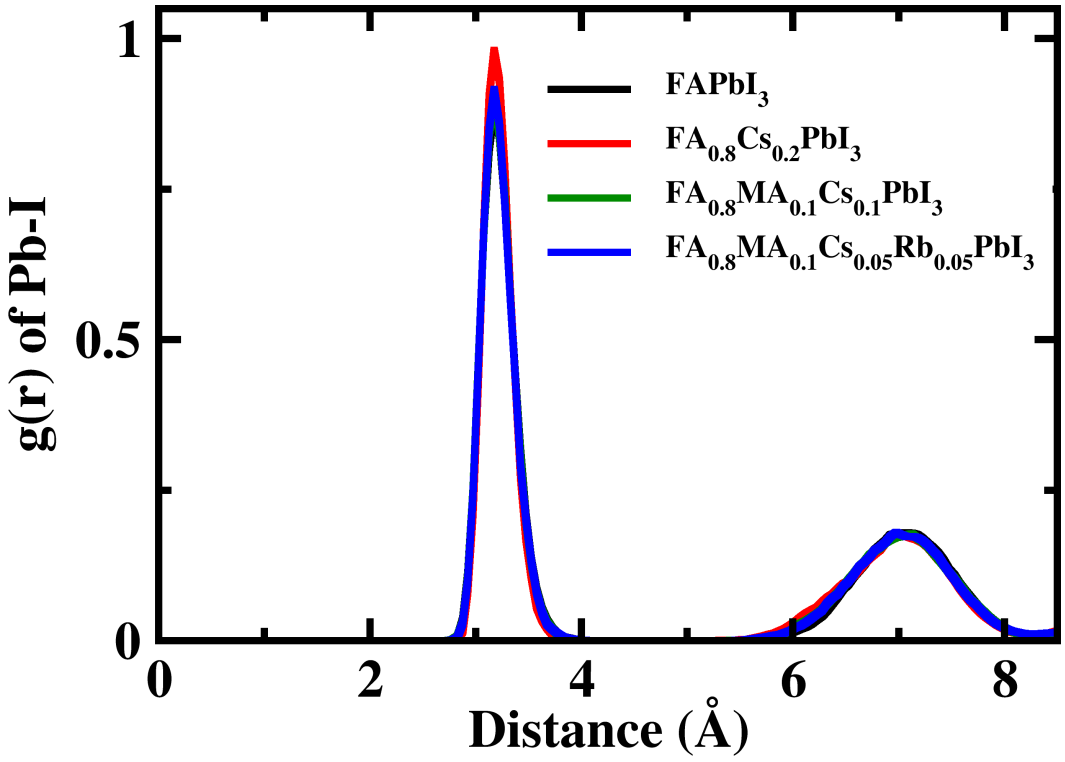

Figure 4.6: Radial distribution function of Pb-I atom pairs in the equilibrated parent $FAPbI_3$ and mixed phases.

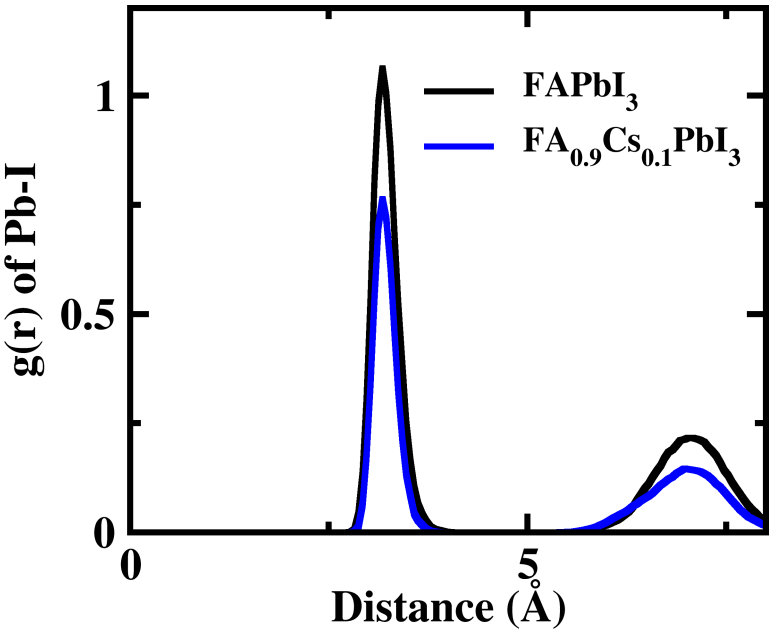

Figure 4.7: Radial distribution function of all Pb-I atom pairs in the equilibrated parent $FAPbI_3$ (black) and octahedra closest to the Cs^+ atom in $FA_{0.9}Cs_{0.1}PbI_3$ (blue).

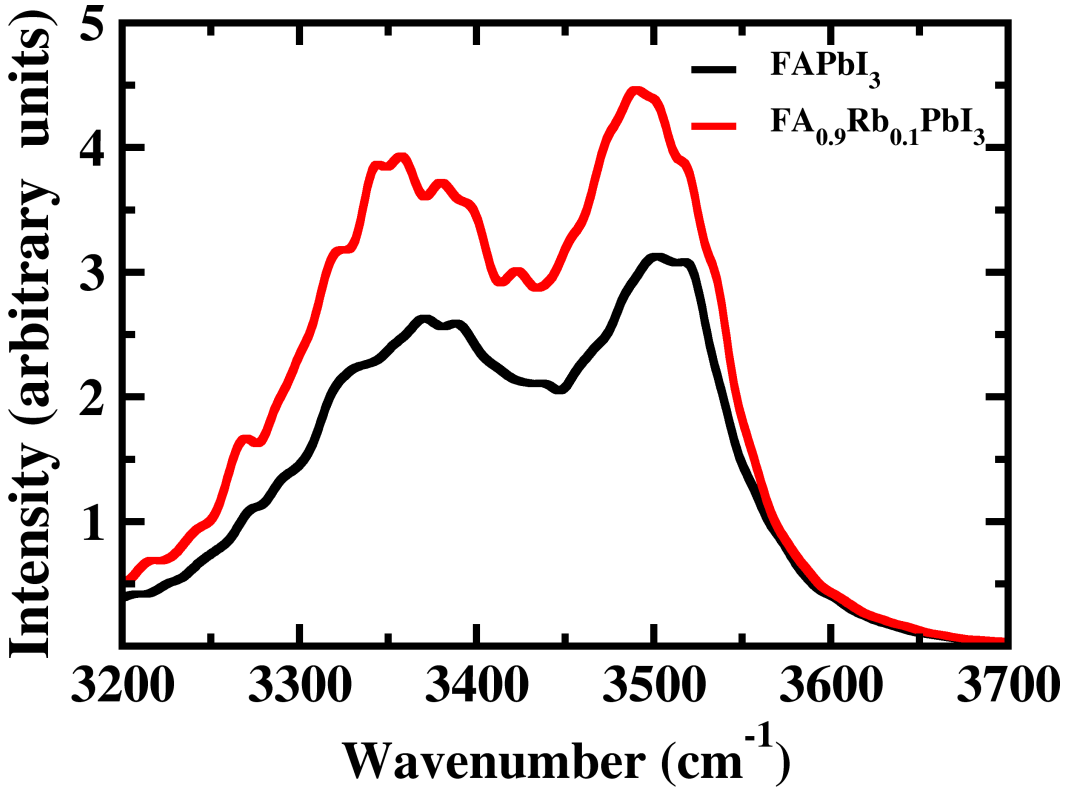

Figure 4.8: Vibrational spectra of FA^+ cations in $FAPbI_3$ (black) and $FA_{0.9}Rb_{0.1}PbI_3$ (red) in the region of the N-H stretching frequency. An increase in intensity and a red shift of the peaks are evident for the mixed A-site cation compound.

These changes in the vibrational spectra and the RDF clearly indicate an increase in the number and strength of N-H–I hydrogen bonds in mixed cation perovskites over the parent phase. This effect is also likely to contribute to the increased perovskite phase stability observed in these mixed cation systems. The reduced fluctuation in hydrogen bond distances due to locked octahedral rocking motion in these perovskites will reduce the fluctuation in the hydrogen bonding itself, and further stabilise the structure. Recent simulation studies on $MAPbI_3$[95,97] also suggest strong NH–I interactions between MA^+ and the Pb-I lattice.

In addition to bonding effects, the 'locking' of the octahedral rotation severely impedes the motion or tumbling of the FA^+ molecular cations in the PbI_6 cages. Recently, several structural and computational studies have demonstrated the coupled dynamical behaviour of 'A' site cations with the surrounding inorganic framework that influences the photovoltaic performance

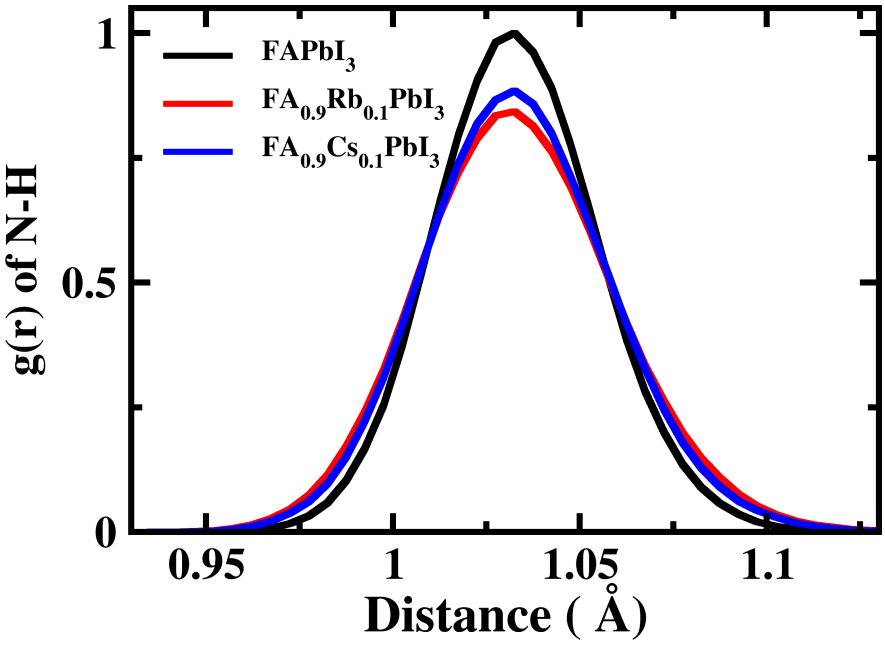

Figure 4.9: Radial distribution function (RDF) of N-H atom pairs in equilibrated parent $FAPbI_3$ (black) and mixed cation $FA_{0.9}A_{0.1}PbI_3$ where A = Cs^+ or Rb^+ (blue/red)

of these halide perovskites.[94,97–103] Molecular rotations in $MAPbBr_3$ have been described as being coupled to $PbBr_6$ octahedral distortions,[94,104] while Selig *et al.*[105] find slower cation dynamics in mixed halide $MAPb(Br,I)_3$.

In the parent FAPI, the FA^+ cation undergoes a tumbling motion with a time constant of 2 ps.[30] To investigate this, we calculated the vector autocorrelation function for the FA^+ cations in all compositions. This measures the probability over time that the orientation of FA^+ cations will remain correlated with the corresponding initial orientation. Physically, it depicts how fast the organic molecular ion rotates inside the inorganic cage. In Figure 4.10 the vector autocorrelation function shows that the doped systems have a higher probability of remaining along the same vector over time than the parent phase. After 6 ps the autocorrelation function for pure undoped FAPI has dropped to 0.1, whereas in the same time period the doped systems only drop to 0.4 and 0.5 for Cs^+ and Rb^+ doped respectively. It can be seen that not just doping has an effect, but the size of the doped cation also affect the degree of autocorrelation.

The time constant, as defined previously as 2 ps, can also be defined as the

time taken for the ion to reach 50 % uncorrelation. For the studied pure system in our investigation this also comes out as 2 ps, in agreement with previous work.[30] For the doped systems, due to the decreased degree of autocorrelation, the time constant can be seen to increase to more than 5 ps. This is further evidence for a significant reduction in the FA^+ tumbling frequency.

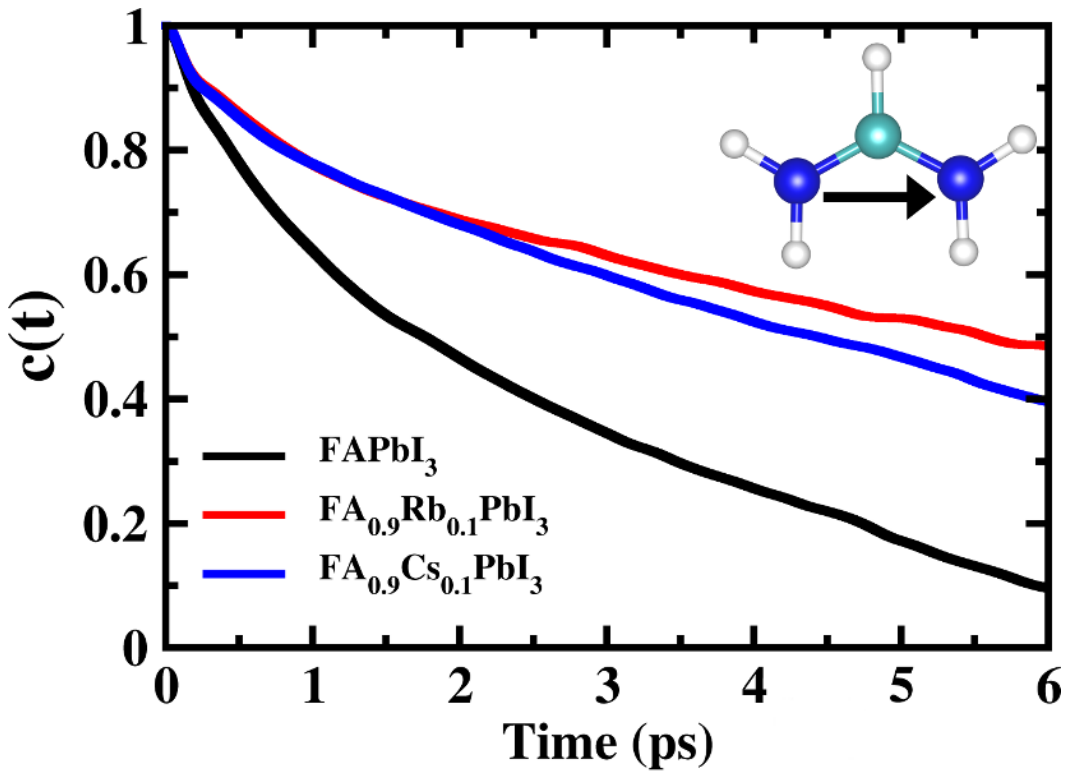

Figure 4.10: The vector autocorrelation function for the FA^+ cations in parent (black) and doped (blue/red) FAPI showing the probability of the cation remaining in the same place over time. Inset is the molecular vector of the FA^+ cation.

Also shown in Figure 4.11 are the nitrogen density plots for FAPI and $FA_{0.9}Cs_{0.1}PbI_3$ in which the positions of the nitrogen atoms have been stacked over time to indicate the main regions occupied. For the parent FAPI, the density plots are almost spherical in nature, indicating rotation and tumbling in all directions with little restriction. In contrast, for the doped system there are two distinct lobes evident in the plot. These lobes relate to the motion of the two individual NH_2^+ groups in the ion and suggests that they mostly remain in a fixed orientation and do not undergo a full rotation in all directions during the simulation.

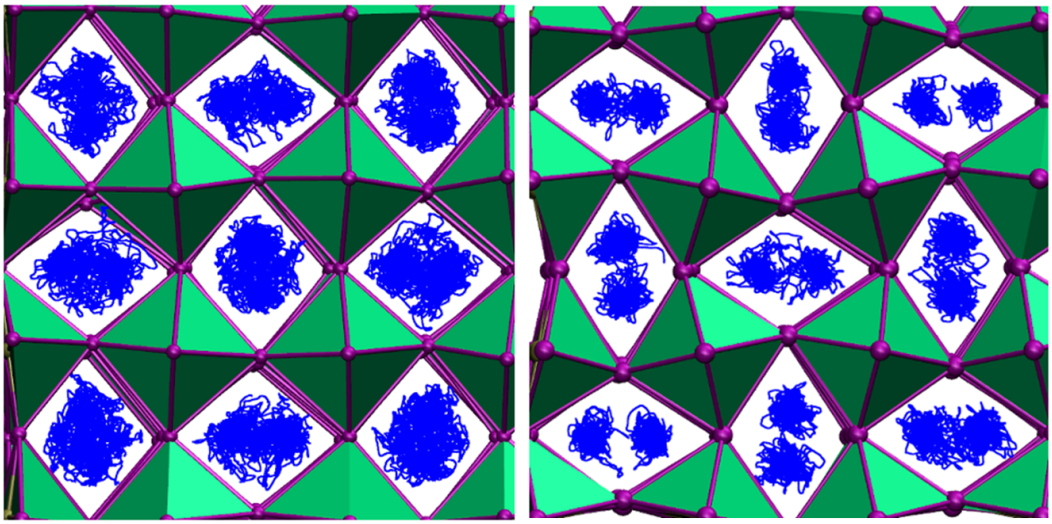

Figure 4.11: Density plots showing positions of the nitrogen atoms of FA^+ accumulated over time (blue) for pure FAPI (Left) and Cs-doped FAPI (Right).

4.2.2 The Effect of Tilting on Photovoltaic Properties

The structural changes as discussed above are particularly significant to the overall investigation into the photovoltaic properties of these perovskites, as the electronic band gap of the materials are associated with Pb-I bond hybridisation. It has previously been shown that the magnitude of the band gap is sensitive to the Pb-I-Pb bond angle, with various studies showing that as the Pb-I-Pb bond angle increases there is a blue-shift in the band gap.[99,106] This study shows that in the mixed cation systems there is a decreased bond angle and the angle undergoes a smaller fluctuation due to the locking. There is reduced electronic disorder in the systems due to this, and doping of the systems can be seen as a way to both vary and control the band gap of the system, making it absorb more monochromatic light. This reduced electronic disorder is a likely reason behind the increased mobility and efficiencies in these mixed cation systems.[107,108] This will need to be quantified in further studies, and the impact on the electronic structure of the perovskite also needs to be studied in more depth, but this is an important stepping stone in the path towards understanding the increases in efficiencies on doping.

4.3 Conclusions

It is known that lead halide perovskites with a mixture of 'A' site cation species show the best solar cell performance, and have higher stability against degradation. This investigation has identified several structural and dynamical features that occur when FAPI is doped with smaller cations such as Cs^+ and Rb^+ on the 'A' site.

1. There is a contraction of the unit cell volume, of up to 2 % for 10 % Rb, which has it's origin in increased tilting of the PbI_6 octahedra to compensate for the reduced space filling by the smaller cations.

2. The oscillation of the tilting in FAPI is significantly reduced with incorporation of smaller cations such as Cs^+ and Rb^+. This indicates that the PbI_6 octahedra become 'locked' and the lattice dynamics are significantly reduced.

3. The rotational or tumbling motion of the organic cations in the cages is restricted by this locking of the PbI_6 framework. The time constant of the tumbling motion of FA^+ cations increases from 2 ps in the pure to 5 ps in the doped systems. There is also an increase in hydrogen bonding (N-H–I) interactions between the organic cation and the surrounding lattice in the mixed systems, which also confers greater structural stability.

These results offer answers to the four fundamental questions arising in relation to tilting, and the origin of the enhancement in solar cell performance can now be understood, and opens up design routes for further study.

4.3.1 Further Work

There are several avenues of further study which arise from this work. The dynamics of the MAPI-FAPI solid solution across a wider range of compositions can be further investigated, with more information still to be gained as to why particular phases of the solid solution are most stable,[56] and where the 'sweet spot' ideal composition lies.

In addition, further work on cation doping can expand on this work, investigating a wider range of 'A' site cations. Further probing how the in-

troduction of very large cations to the structure affects the properties of the device, such as guanidinium ($(C(NH_2)_3{}^+$) is of increasing interest in the community,[109,110] and the methods used in this investigation could provide the answers to fundamental questions about the dynamics of these systems.

Finally, using the knowledge acquired about tuning the band gaps of these materials, this investigation can be furthered by determining the ideal composition of multication perovskites for photovoltaic applications, which can then be used to inform experiment in the endeavour to find the most efficient solar cell.

Chapter 5

Conclusions

"There was a point to this story, but it has temporarily escaped the chronicler's mind"

Douglas Adams
So Long, and Thanks for All the Fish

In this investigation there were two main aims: Firstly to develop an interatomic potential for the $Cs(Pb,Sn)(I,Br,Cl)_3$ series, and secondly to understand 'A' site doping in these materials. Underpinning both aims was a desire to further understand the properties of these materials and gain an understanding of how we can improve their viability for use in solar cells.

Using $CsPbI_3$ as a base, an interatomic potential model for the $Cs(Pb,Sn)(I,Br,Cl)_3$ series has been successfully developed, utilising Morse potentials. This model is able to very accurately model the bulk properties of both the perovskite and non-perovskite phases of each member of the series to a very high degree of accuracy, and can therefore be used to determine useful information about relative phase stabilities. This information paints a picture of why the non-perovskite phase of $CsPbI_3$ is stable at room temperature over the perovskite phase. Building from this the model also shows how stabilisation of the perovskite phase can be achieved by varying the size of the 'A' site cation. It was seen that increasing the average ionic radius of the 'A' site cation by doping with larger ions stabilises the perovskite phase and this is the case in MAPI-FAPI solid solutions, showcasing their suitability as potential photovoltaics.

To understand 'A' site doping in these materials and get a greater understanding of how the efficiency of perovskite solar cells varies on cation doping MD simulations were carried out on FAPI and on doped FAPI systems. Phenomena such as the tilting of the PbI_6 octahedra and octahedral locking were the main focus of this section of the project. The investigation identified several structural and dynamical features that occur when FAPI is doped with smaller cations and sheds light onto the efficacy of the doped FAPI systems as photovoltaics.

On doping, a contraction of the unit cell volume was seen, originating with increased tilting of the PbI_6 octahedra as the introduction of smaller cations into the lattice is compensated for. There was also significantly reduced tilting motion seen with incorporation of smaller cations onto the 'A' site. This was indicative of the 'locking' of the PbI_6 octahedra. The locking was then seen to restrict the rotational motion of the organic cations in the cages, and increase the time constant of the tumbling motion from 2 ps in the pure to 5 ps in the doped systems. There is also an increase in hydrogen bonding (N-H–I) interactions between the organic cation and the surrounding lattice on doping.

These results shed light on the fundamental processes that make these materials good photovoltaics, and also provides a starting point for further research in the area.

Appendix A

The Glazer Tilt System

A classification system for the possible tilts in perovskite structures was developed by Glazer with 23 possible tilt systems suggested.[18,19,111] In a tilt system, there can be between zero and three tilts around three axes, with the fully symmetrical cubic system having zero and more tilts being present with decreasing symmetry.

When describing tilts along each axis in a system, the magnitude of each tilt is defined in relation to the tilts on the other two axes – with 'aaa' meaning equal tilts on each axis, 'aab' meaning equal tilts on two axes but different on the z axis and 'abc' meaning three unequal tilts. Tilts about an axis on adjacent layers in the structure can either be in phase or antiphase, notated with a '+' or a '-'. If there is no tilting present on an axis then 'a0' is used to denote this.[18,19]

Each of the 23 different tilt systems has a defined space group associated with it, and as a result knowledge of the tilt system can be used to determine the symmetry and vice versa. This notation holds true for the vast majority of known perovskite systems, with some exceptions where the symmetry is dominated by either Jahn-Teller distortions or there are combinations of the systems present.[19] Table A.1 describes the 23 tilt patterns and the rules governing them.

The 23 Glazer tilt systems have been examined further by Woodward (1997) who determined that in not all of the systems it was possible to produce a 3D framework without additional distortions in the lattice.[112,113] Howard and Stokes (1998 and 2005) use group theory to identify 15 tilt systems as unique, and describe the phase transitions between them.[114,115]

Table A.1: Tilt Systems in perovskites with Glazer notation from Glazer,[18,111] and Woodward[112,113]

Tilts	Number	Symbol	Centring	Space Group	Parameters
3	1	$a^+b^+c^+$	I	$Immm$	a≠b≠c
”	2	$a^+b^+b^+$	I	$Immm$	a≠b=c
”	3	$a^+a^+a^+$	I	$Im-3$	a=b=c
”	4	$a^+b^+c^-$	P	$Pmmn$	a≠b≠c
”	5	$a^+a^+c^-$	P	$P42/nmc$	a=b≠c
”	6	$a^+b^+b^-$	P	$Pmmn$	a≠b=c
”	7	$a^+a^+a^-$	P	$P42/nmc$	a=b=c
”	8	$a^+b^-\ c^-$	A	$P21/m$	a≠b≠c $\alpha \neq 90°$
”	9	$a^+a^-\ c^-$	A	$P21/m$	a=b≠c $\alpha \neq 90°$
”	10	a^+b^+b-	A	Pnma	a≠b=c $\alpha \neq 90°$
”	11	$a^+a^-\ a^-$	A	$Pnma$	a=b=c $\alpha \neq 90°$
”	12	$a^-b^-c^-$	F	$P-1$	a≠b≠c $\alpha \neq 90°\beta \neq 90°\gamma \neq 90°$
”	13	$a^-b^-b^-$	F	$C2/c$	a≠b=c $\alpha \neq 90°\beta \neq 90°\gamma \neq 90°$
”	14	$a^-a^-a^-$	F	$R-3c$	a=b=c $\alpha \neq 90°\beta \neq 90°\gamma \neq 90°$
2	15	$a0b^+c^+$	I	$Immm$	a<b≠c
”	16	$a0b^+b^+$	I	$P43$	a<b=c
”	17	$a0b^+c^-$	B	$Cmcm$	a<b≠c
”	18	$a0b^+b^-$	B	$Cmcm$	a<b=c
”	19	$a0b^-c^-$	F	$C2/m$	a<b≠c $\alpha \neq 90°$
”	20	$a0b^-b^-$	F	$Imma$	a<b=c $\alpha \neq 90°$
1	21	$a0a0c^+$	C	$P4/mbm$	a=b<c
”	22	$a0a0c^-$	F	$I4/mcm$	a=b<c
0	23	a0a0a0	P	$Pm-3m$	a=b=c

As shown in Figure A.1, there are both ferroelastic (in red) and nonferroelastic (blue) phase transitions. There are also certain phases each system has to go between in order to change between two different tilt systems.

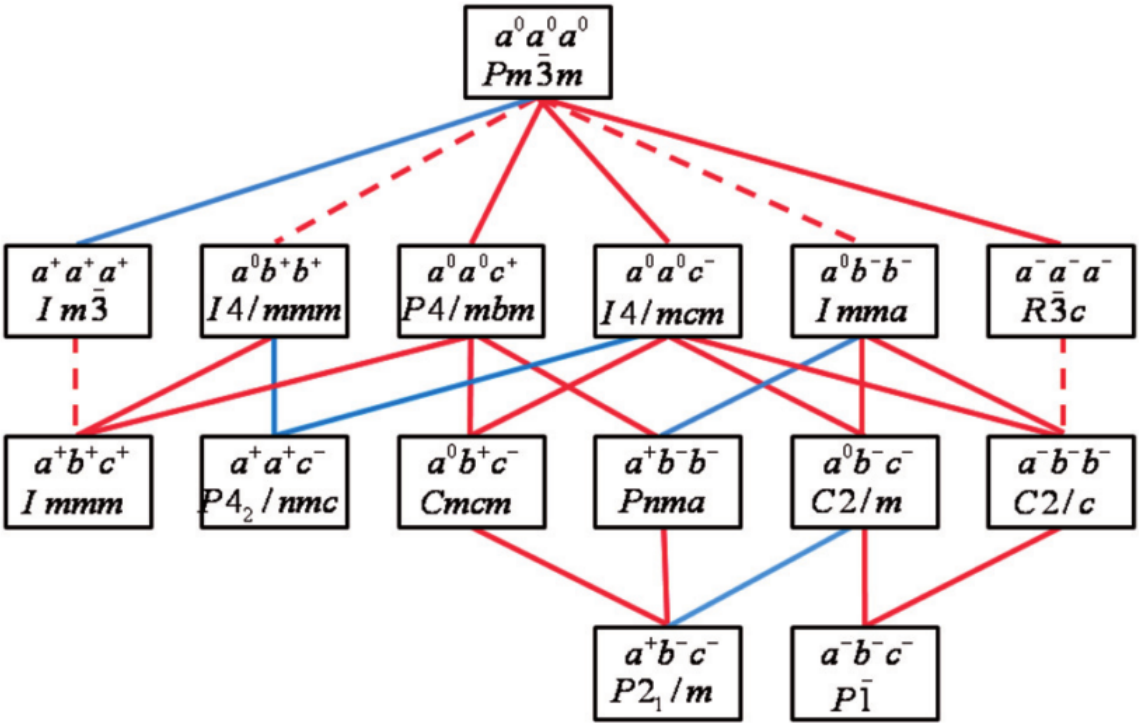

Figure A.1: The 15 possible tilt systems and the relationship between them. From Glazer[111]. Showing ferroelastic (red) and nonferroelastic (blue) phase transitions

Bibliography

[1] J. Peng, L. Lu and H. Yang, *Renewable and Sustainable Energy Reviews*, 2013, **19**, 255–274.

[2] D. M. Chapin, C. S. Fuller and G. L. Pearson, *Journal of Applied Physics*, 1954, **25**, 676–677.

[3] R. W. Miles, K. M. Hynes and I. Forbes, *Progress in Crystal Growth and Characterization of Materials*, 2005, **51**, 1–42.

[4] R. W. Miles, *Vacuum*, 2006, **80**, 1090–1097.

[5] A. Goetzberger, C. Hebling and H.-W. Schock, *Materials Science and Engineering: R: Reports*, 2003, **40**, 1–46.

[6] P. Sinha, *Solar Energy Materials and Solar Cells*, 2013, **119**, 271–275.

[7] B. O'Regan and M. Grätzel, *Nature*, 1991, **353**, 737–740.

[8] H. Katagiri, K. Saitoh, T. Washio, H. Shinohara, T. Kurumadani and S. Miyajima, *Solar Energy Materials and Solar Cells*, 2001, **65**, 141–148.

[9] M. T. Winkler, W. Wang, O. Gunawan, H. J. Hovel, T. K. Todorov and D. B. Mitzi, *Energy & Environmental Science*, 2014, **7**, 1029.

[10] A. Kojima, K. Teshima, Y. Shirai and T. Miyasaka, *Journal of the American Chemical Society*, 2009, **131**, 6050–6051.

[11] M. M. Lee, J. Teuscher, T. Miyasaka, T. N. Murakami and H. J. Snaith, *Science*, 2012, **338**, 643–647.

[12] W. S. Yang, J. H. Noh, N. J. Jeon, Y. C. Kim, S. Ryu, J. Seo and S. I. Seok, *Science*, 2015, **348**, 1234–1237.

[13] R. J. Sutton, G. E. Eperon, L. Miranda, E. S. Parrott, B. A. Kamino, J. B. Patel, M. T. Hörantner, M. B. Johnston, A. A. Haghighirad, D. T. Moore and H. J. Snaith, *Advanced Energy Materials*, 2016, 1502458.

[14] C. C. Stoumpos, C. D. Malliakas and M. G. Kanatzidis, *Inorganic Chemistry*, 2013, **52**, 9019–9038.

[15] M. Kulbak, D. Cahen and G. Hodes, *The Journal of Physical Chemistry Letters*, 2015, **6**, 2452–2456.

[16] G. E. Eperon, G. M. Paternò, R. J. Sutton, A. Zampetti, A. A. Haghighirad, F. Cacialli and H. J. Snaith, *J. Mater. Chem. A*, 2015, **3**, 19688–19695.

[17] C. Eames, J. M. Frost, P. R. F. Barnes, B. C. O'Regan, A. Walsh and M. S. Islam, *Nature Communications*, 2015, **6**, 7497.

[18] A. M. Glazer, *Acta Crystallographica Section B Structural Crystallography and Crystal Chemistry*, 1972, **28**, 3384–3392.

[19] A. M. Glazer, *Acta Crystallographica Section A*, 1975, **31**, 756–762.

[20] Q. Ma, S. Huang, X. Wen, M. A. Green and A. W. Y. Ho-Baillie, *Advanced Energy Materials*, 2016, 1502202.

[21] S. J. Lee, S. S. Shin, Y. C. Kim, D. Kim, T. K. Ahn, J. H. Noh, J. Seo and S. I. Seok, *Journal of the American Chemical Society*, 2016, **138**, 3974–3977.

[22] R. E. Beal, D. J. Slotcavage, T. Leijtens, A. R. Bowring, R. A. Belisle, W. H. Nguyen, G. F. Burkhard, E. T. Hoke and M. D. McGehee, *The Journal of Physical Chemistry Letters*, 2016, **7**, 746–751.

[23] C. Yi, J. Luo, S. Meloni, A. Boziki, N. Ashari-Astani, C. Grätzel, S. M. Zakeeruddin, U. Röthlisberger and M. Grätzel, *Energy Environ. Sci.*, 2016, **9**, 656–662.

[24] Y. Chen, B. Li, W. Huang, D. Gao and Z. Liang, *Chem. Commun.*, 2015, **51**, 11997–11999.

[25] J. Burschka, N. Pellet, S.-J. Moon, R. Humphry-Baker, P. Gao, M. K. Nazeeruddin and M. Grätzel, *Nature*, 2013, **499**, 316–319.

[26] J. Seo, J. H. Noh and S. I. Seok, *Accounts of Chemical Research*, 2016, **49**, 562–572.

[27] N. J. Jeon, J. H. Noh, W. S. Yang, Y. C. Kim, S. Ryu, J. Seo and S. I. Seok, *Nature*, 2015, **517**, 476–480.

[28] J. H. Heo and S. H. Im, *Nanoscale*, 2016, **8**, 2554–2560.

[29] M. Saliba, T. Matsui, J.-Y. Seo, K. Domanski, J.-P. Correa-Baena, M. K. Nazeeruddin, S. M. Zakeeruddin, W. Tress, A. Abate, A. Hagfeldt and M. Grätzel, *Energy Environ. Sci.*, 2016, **9**, 1989–1997.

[30] M. T. Weller, O. J. Weber, J. M. Frost and A. Walsh, *The Journal of Physical Chemistry Letters*, 2015, **6**, 3209–3212.

[31] D. Trots and S. Myagkota, *Journal of Physics and Chemistry of Solids*, 2008, **69**, 2520–2526.

[32] K. Yamada, S. Funabiki, H. Horimoto, T. Matsui, T. Okuda and S. Ichiba, *Chemistry Letters*, 1991, **20**, 801–804.

[33] I. Chung, J.-H. Song, J. Im, J. Androulakis, C. D. Malliakas, H. Li, A. J. Freeman, J. T. Kenney and M. G. Kanatzidis, *Journal of the American Chemical Society*, 2012, **134**, 8579–8587.

[34] M. Rodová, J. Brožek, K. Knížek and K. Nitsch, *Journal of Thermal Analysis and Calorimetry*, 2003, **71**, 667–673.

[35] C. C. Stoumpos, C. D. Malliakas, J. a. Peters, Z. Liu, M. Sebastian, J. Im, T. C. Chasapis, A. C. Wibowo, D. Y. Chung, A. J. Freeman, B. W. Wessels and M. G. Kanatzidis, *Crystal Growth & Design*, 2013, **13**, 2722–2727.

[36] J. D. Donaldson, J. Silver, S. Hadjiminolis and S. D. Ross, *Journal of the Chemical Society, Dalton Transactions*, 1975, 1500.

[37] F. Somma, M. Nikl, K. Nitsch, P. Fabeni and G. P. Pazzi, *Journal of Luminescence*, 2001, **94-95**, 169–172.

[38] L. Lang, J.-H. Yang, H.-R. Liu, H. Xiang and X. Gong, *Physics Letters A*, 2014, **378**, 290–293.

[39] Y. H. Chang, C. H. Park and K. Matsuishi, *Journal of the Korean Physical Society*, 2004, **44**, 889–893.

[40] R. A. Jishi, O. B. Ta and A. A. Sharif, *J. Phys. Chem. C*, 2014, **118**, 28344–28349.

[41] J. Mizusaki, K. Arai and K. Fueki, *Solid State Ionics*, 1983, **11**, 203–211.

[42] R. L. Narayan, M. V. S. Sarma and S. V. Suryanarayana, *Journal of Materials Science Letters*, 1987, **6**, 93–94.

[43] R. Narayan and S. Suryanarayana, *Materials Letters*, 1991, **11**, 305–308.

[44] T. A. Kuku and A. M. Salau, *Solid State Ionics*, 1987, **25**, 1–7.

[45] T. A. Kuku, E. R. Chioba, G. Chiodelli, E. Engineering, C. Fisica and S. S. Fusi, *Solid State Ionics*, 1989, **34**, 141–147.

[46] S. Meloni, T. Moehl, W. Tress, M. Franckevičius, M. Saliba, Y. H. Lee, P. Gao, M. K. Nazeeruddin, S. M. Zakeeruddin, U. Rothlisberger and M. Graetzel, *Nature Communications*, 2016, **7**, 10334.

[47] K. Nitsch, V. Hamplová, M. Nikl, K. Polák and M. Rodová, *Chemical Physics Letters*, 1996, **258**, 518–522.

[48] M. Nikl, E. Mihokova, K. Nitsch, K. Polak, M. Rodova, M. Dusek, G. P. Pazzi, P. Fabeni, L. Salvini and M. Gurioli, *Chemical Physics Letters*, 1994, **220**, 14–18.

[49] S. Kondo, H. Nakagawa, T. Saito and H. Asada, *Current Applied Physics*, 2004, **4**, 439–444.

[50] K. Nitsch, M. Dušek, M. Nikl, K. Polák and M. Rodová, *Progress in Crystal Growth and Characterization of Materials*, 1995, **30**, 1–22.

[51] B. Conings, J. Drijkoningen, N. Gauquelin, A. Babayigit, J. D'Haen, L. D'Olieslaeger, A. Ethirajan, J. Verbeeck, J. Manca, E. Mosconi, F. D. Angelis and H. Boyen, *Advanced Energy Materials*, 2015, **5**, 1500477.

[52] B. Philippe, B.-W. Park, R. Lindblad, J. Oscarsson, S. Ahmadi, E. M. J. Johansson and H. Rensmo, *Chemistry of Materials*, 2015, **27**, 1720–1731.

[53] J. Yang, B. D. Siempelkamp, E. Mosconi, F. De Angelis and T. L. Kelly, *Chemistry of Materials*, 2015, **27**, 4229–4236.

[54] N. Pellet, P. Gao, G. Gregori, T. Y. Yang, M. K. Nazeeruddin, J. Maier and M. Gratzel, *Angew. Chem. Int. Ed.*, 2014, **53**, 3151–3157.

[55] M. Saliba, T. Matsui, K. Domanski, J.-Y. Seo, A. Ummadisingu, S. M. Zakeeruddin, J.-P. Correa-Baena, W. R. Tress, A. Abate, A. Hagfeldt and M. Gratzel, *Science*, 2016, **354**, 206–209.

[56] O. J. Weber, B. Charles and M. T. Weller, *J. Mater. Chem. A*, 2016, **4**, 15375–15382.

[57] T. Matsui, J. Seo, M. Saliba, S. M. Zakeeruddin and M. Grätzel, *Advanced Materials*, 2017, **29**, 1606258.

[58] D. P. McMeekin, G. Sadoughi, W. Rehman, G. E. Eperon, M. Saliba, M. T. Hörantner, A. Haghighirad, N. Sakai, L. Korte, B. Rech, M. B. Johnston, L. M. Herz and H. J. Snaith, *Science*, 2016, **351**, 151–155.

[59] O. A. Syzgantseva, M. Saliba, M. Grätzel and U. Rothlisberger, *The Journal of Physical Chemistry Letters*, 2017, **8**, 1191–1196.

[60] Z. Li, M. Yang, J. S. Park, S. H. Wei, J. J. Berry and K. Zhu, *Chemistry of Materials*, 2016, **28**, 284–292.

[61] L.-Q. Xie, L. Chen, Z.-A. Nan, H.-X. Lin, T. Wang, D.-P. Zhan, J.-W. Yan, B.-W. Mao and Z.-Q. Tian, *J. Am. Chem. Soc.*, 2017, **139**, 3320–3323.

[62] X. Zheng, C. Wu, S. K. Jha, Z. Li, K. Zhu and S. Priya, *ACS Energy Lett.*, 2016, **1**, 1014–1020.

[63] C. R. A. Catlow, *Computer Modelling in Inorganic Crystallography*, Academic Press, 1997.

[64] A. R. Leach, *Molecular Modelling Principles and Applications*, Pearson Education, 2nd edn, 2001.

[65] G. V. Lewis and C. R. A. Catlow, *Journal of Physics C: Solid State Physics*, 1985, **18**, 1149–1161.

[66] M. S. Islam, D. J. Driscoll, C. A. J. Fisher and P. R. Slater, *Chemistry of Materials*, 2005, **17**, 5085–5092.

[67] J. A. Dawson, X. Li, C. L. Freeman, J. H. Harding and D. C. Sinclair, *Journal of Materials Chemistry C*, 2013, **1**, 1574.

[68] M. S. Islam and C. A. J. Fisher, *Chem. Soc. Rev.*, 2014, **43**, 185–204.

[69] M. Fyta, *Computational Approaches in Physics*, Morgan & Claypool, 2016.

[70] B. G. Dick and A. W. Overhauser, *Physical Review*, 1958, **112**, 90–103.

[71] J. D. Gale, *Journal of the Chemical Society, Faraday Transactions*, 1997, **93**, 629–637.

[72] J. D. Gale and A. L. Rohl, *Molecular Simulation*, 2003, **29**, 291–341.

[73] N. F. Mott and M. J. Littleton, *Transactions of the Faraday Socety*, 1938, **34**, 485–499.

[74] S. Plimpton, *Journal of Computational Physics*, 1995, **117**, 1–19.

[75] J. Hutter, M. Iannuzzi, F. Schiffmann and J. VandeVondele, *Wiley Interdisciplinary Reviews: Computational Molecular Science*, 2014, **4**, 15–25.

[76] M. J. Sangster, R. M. Atwood and U. Schroder, *Journal of Physics C: Solid State Physics*, 1978, **11**, 1523.

[77] M. J. L. Sangster and R. M. Atwood, *Journal of Physics C: Solid State Physics*, 2001, **11**, 1541–1555.

[78] C. R. A. Catlow, K. M. Diller and M. J. Norgett, *Journal of Physics C: Solid State Physics*, 1977, **10**, 1395–1412.

[79] M. S. Islam, *Journal of Solid State Chemistry*, 1990, **85**, 251–261.

[80] A. Mattoni, A. Filippetti, M. I. Saba and P. Delugas, *The Journal of Physical Chemistry C*, 2015, **119**, 17421–17428.

[81] R. S. Mulliken, *The Journal of Chemical Physics*, 1955, **23**, 1833–1840.

[82] G. Kresse and J. Furthmüller, *Physical Review B*, 1996, **54**, 11169–11186.

[83] A. Verma and A. Kumar, *Journal of Alloys and Compounds*, 2012, **541**, 210–214.

[84] A. C. T. van Duin, S. Dasgupta, F. Lorant and W. A. Goddard, *The Journal of Physical Chemistry A*, 2001, **105**, 9396–9409.

[85] A. M. Salau, *Solar Energy Materials*, 1980, **2**, 327–332.

[86] P. Gao, M. Grätzel and M. K. Nazeeruddin, *Energy Environ. Sci.*, 2014, **7**, 2448–2463.

[87] E. T. McClure, M. R. Ball, W. Windl and P. M. Woodward, *Chemistry of Materials*, 2016, **28**, 1348–1354.

[88] G. Volonakis, M. R. Filip, A. A. Haghighirad, N. Sakai, B. Wenger, H. J. Snaith and F. Giustino, *The Journal of Physical Chemistry Letters*, 2016, **7**, 1254–1259.

[89] H. Tsai, W. Nie, J.-C. Blancon, C. C. Stoumpos, R. Asadpour, B. Harutyunyan, A. J. Neukirch, R. Verduzco, J. J. Crochet, S. Tretiak, L. Pedesseau, J. Even, M. A. Alam, G. Gupta, J. Lou, P. M. Ajayan, M. J. Bedzyk, M. G. Kanatzidis and A. D. Mohite, *Nature*, 2016.

[90] M. R. Filip, G. E. Eperon, H. J. Snaith and F. Giustino, *Nature Communications*, 2014, **5**, 5757.

[91] L. D. Whalley, J. M. Frost, Y.-K. Jung and A. Walsh, *The Journal of Chemical Physics*, 2017, **146**, 220901.

[92] F. Brivio, J. M. Frost, J. M. Skelton, A. J. Jackson, O. J. Weber, M. T. Weller, A. R. Goñi, A. M. A. Leguy, P. R. F. Barnes and A. Walsh, *Physical Review B*, 2015, **92**, 144308.

[93] J. Young and J. M. Rondinelli, *J. Phys. Chem. Lett*, 2016, **7**, 918–922.

[94] A. Bernasconi and L. Malavasi, *ACS Energy Letters*, 2017, **2**, 863–868.

[95] Z. Zhou, S. Pang, F. Ji, B. Zhang and G. Cui, *Chem. Commun.*, 2016, **52**, 3828–3831.

[96] T. Glaser, C. Müller, M. Sendner, C. Krekeler, O. E. Semonin, T. D. Hull, O. Yaffe, J. S. Owen, W. Kowalsky, A. Pucci and R. Lovrinčić, *The Journal of Physical Chemistry Letters*, 2015, **6**, 2913–2918.

[97] J. S. Bechtel, R. Seshadri and A. Van der Ven, *The Journal of Physical Chemistry C*, 2016, **120**, 12403–12410.

[98] J.-H. Lee, N. C. Bristowe, J. H. Lee, S.-H. Lee, P. D. Bristowe, A. K. Cheetham and H. M. Jang, *Chemistry of Materials*, 2016, **28**, 4259–4266.

[99] A. Amat, E. Mosconi, E. Ronca, C. Quarti, P. Umari, M. K. Nazeeruddin, M. Grätzel and F. De Angelis, *Nano Letters*, 2014, **14**, 3608–3616.

[100] J. M. Frost, K. T. Butler, F. Brivio, C. H. Hendon, M. Van Schilfgaarde and A. Walsh, *Nano Letters*, 2014, **14**, 2584–2590.

[101] M. T. Weller, O. J. Weber, P. F. Henry, A. M. Di Pumpo and T. C. Hansen, *Chem. Commun.*, 2015, **51**, 4180–4183.

[102] T. Chen, B. J. Foley, B. Ipek, M. Tyagi, J. R. D. Copley, C. M. Brown, J. J. Choi and S.-H. Lee, *Phys. Chem. Chem. Phys.*, 2015, **17**, 31278–31286.

[103] B. Kang and K. Biswas, *The Journal of Physical Chemistry C*, 2017, **121**, 8319–8326.

[104] T. Hata, G. Giorgi, K. Yamashita, C. Caddeo and A. Mattoni, *The Journal of Physical Chemistry C*, 2017, **121**, 3724–3733.

[105] O. Selig, A. Sadhanala, C. Muller, R. Lovrincic, Z. Chen, Y. L. A. Rezus, J. M. Frost, T. L. C. Jansen and A. A. Bakulin, *J. Am. Chem. Soc.*, 2017, **139**, 4068–4074.

[106] C. C. Stoumpos and M. G. Kanatzidis, *Accounts of Chemical Research*, 2015, **48**, 2791–2802.

[107] W. Rehman, D. P. McMeekin, J. B. Patel, R. L. Milot, M. B. Johnston, H. J. Snaith and L. M. Herz, *Energy Environ. Sci.*, 2017, **10**, 361–369.

[108] Y. Huang, L. Li, Z. Liu, H. Jiao, Y. He, X. Wang, R. Zhu, D. Wang, J. Sun and Q. Chen, *J. Mater. Chem. A*, 2017, **5**, 8537–8544.

[109] G. Giorgi, J. I. Fujisawa, H. Segawa and K. Yamashita, *Journal of Physical Chemistry C*, 2015, **119**, 4694–4701.

[110] M. Becker, T. Klüner and M. Wark, *Dalton Trans.*, 2017, **46**, 3500–3509.

[111] A. M. Glazer, *Phase Transitions*, 2011, **84**, 405–420.

[112] P. M. Woodward, *Acta Crystallographica B*, 1997, **53**, 32–43.

[113] P. M. Woodward, *Acta Crystallographica B*, 1997, **53**, 44–66.

[114] C. J. Howard and H. T. Stokes, *Acta Crystallographica Section B Structural Science*, 1998, **54**, 782–789.

[115] C. J. Howard and H. T. Stokes, *Acta Crystallographica Section A*, 2005, **61**, 93–111.

"I may not have gone where I intended to go, but I think I have ended up where I intended to be."

Douglas Adams